Optimization of the Alignment Method for an Electric Vehicle Magnetic Field Wireless Power Transfer System Using a Low-Frequency Ferrite Rod Antenna

Jae Yong Seong and **Sang-Sun Lee** *

Department of Electronics and Computer Engineering, Hanyang University, Seoul 04763, Korea; jyseong@hyundai.com
* Correspondence: ssnlee@hanyang.ac.kr; Tel.: +82-2-2299-0372

check for updates

Abstract: The establishment of international and regional standards for electric vehicle (EV) magnetic field wireless power transfer (MF-WPT) systems started in 2010 by the Society of Automotive Engineers (SAE). In the meantime, the EV MF-WPT standardization has been focused on primary device and secondary device topology. Recently, the International Organization for Standardization (ISO), the International Electrotechnical Commission (IEC), and SAE have begun describing the communication and alignment techniques for EV MF-WPT. In this paper, we present a fine positioning method using a low-frequency (LF) signal, as mentioned in IEC 61980 and SAE J2954. Through modeling and simulation, we optimized a LF ferrite rod antenna (FRA) for EV MF-WPT fine positioning. We also found the optimal arrangement of LF-FRAs on primary device and secondary device Finally, we used a test bench to experiment and check the results of our proposal.

Keywords: electric vehicle; wireless power transfer; MF-WPT; alignment; fine positioning; LF signal; LF-FRA

---

1. Introduction

Wireless power transfer (WPT) was first experimented upon by Nikola Tesla at the end of the 1800s; WPT is a technology for transmitting electric energy through the air without using wires [1]. The early days of WPT were not commercialized, except for non-contact-type inductive coupling methods because of WPT's technological limitations and potential danger to the human body. However, in 2007, Marin Soljacic (a professor at MIT) proposed a new non-radiated magnetic resonance method [2] for wireless power transfer. Subsequently, various methods of WPT technology have been researched and developed. Recently, in the field of electric mobile devices (including smartphones), the demand for wireless charging has rapidly increased, and the wireless charging market is also rapidly growing [3].

The research and development of WPT technology are currently underway in the automotive field. Since the beginning of the 2000s, as a response to the strengthening of environmental regulations in automotive divisions, consideration for the environment has increased interest in low-carbon vehicles. Keeping pace with this, developed countries also began to mass-produce eco-friendly vehicles. Thus, the paradigm of the global automotive market is changing from internal combustion engines to environmental vehicles, with a focus on electric vehicles (EVs). As electric vehicles become increasingly commercialized, offering the convenience of charging, interest in wireless charging for electric vehicles that is safe from short-circuiting and the disconnection of charging cables has also increased.

The de jure international standards for electric vehicle magnetic field wireless power transfer (EV MF-WPT) are the International Organization for Standardization (ISO)/technical committees (TC) 22/sub-committees (SC) 37/working group (WG) 1 19363 [4], the International Electrotechnical

Commission (IEC)/TC 69/WG7 61980 [5], the ISO/TC22/SC31/joint working group (JWG) 1 15118 [6], and IEC/TC69/JWG1 15118 [7]. Similarly, the de facto regional standards for EV MF-WPT are the Society of Automotive Engineers (SAE) wireless power transfer and alignment task force [8] and the SAE hybrid communication and interoperability task force [9]. These three organizations are currently under consideration and aim to establish standards by 2020.

In this paper, we designed and modeled an optimized arrangement of a low-frequency (LF) ferrite rod antenna (FRA) for the fine positioning of an EV MF-WPT in accordance with IEC 61980 [10–12] and SAE J2954 [13] standards. To develop the LF-FRA modeling and electrical schematics of the EV MF-WPT system, we used simulation software that is widely used in industry and academia. Our contributions are as follows:

(i)　We designed and modeled the LF-FRA to be used for the fine positioning of an EV MF-WPT. In addition, optimization was performed to integrate the LF-FRA into the primary device and the secondary device.

(ii)　We simulated an array of LF-FRAs to be integrated into the primary device and the secondary device in order to determine which B-field recognition distance was the longest during fine positioning. In addition, the LF-FRA, which acted as a receiver even if the B field of the LF-FRA of the primary device overlaps with the B field of the secondary device, simulated the optimum position of the LF-FRA to ensure that the distance was accurately recognized.

(iii)　We built a test bench for fine positioning and performed experiments based on simulated results to verify our proposal.

This paper is organized as follows. In Section 2, we describe the international and regional standards related to WPT. In Section 3, we explain the theoretical background. In Section 4, the pre-conditions for the fine positioning of the EV MF-WPT are established. In Section 5, we perform modeling and simulations to confirm the optimal conditions. In Section 6, we use a test bench to verify our proposal. We conclude in Section 7. Finally, in Appendices A and B, we describe the details of results that were not explained in the body of the paper.

2. Background: Electric Vehicle Magnetic Field Wireless Power Transfer Systems and Standards

In this section, we introduce the system and architecture of an EV MF-WPT. We describe the contents defined in the relevant international standards and regional standards and explain the related EV MF-WPT standards. Further, we describe not only the alignment methodologies defined in the standards but also the mechanisms. In the following section, we discuss the EV MF-WPT standards in more detail.

2.1. EV MF-WPT System Components

According to ISO 19363 [14] and IEC 61980 [10–12], an EV MF-WPT system is defined by the wireless transfer of energy from a power source to an electrical load via a magnetic field. EV MF-WPT systems consist of the supply device and the EV device, as shown in Figure 1 [12–14]. Each device can be divided into three sub-systems.
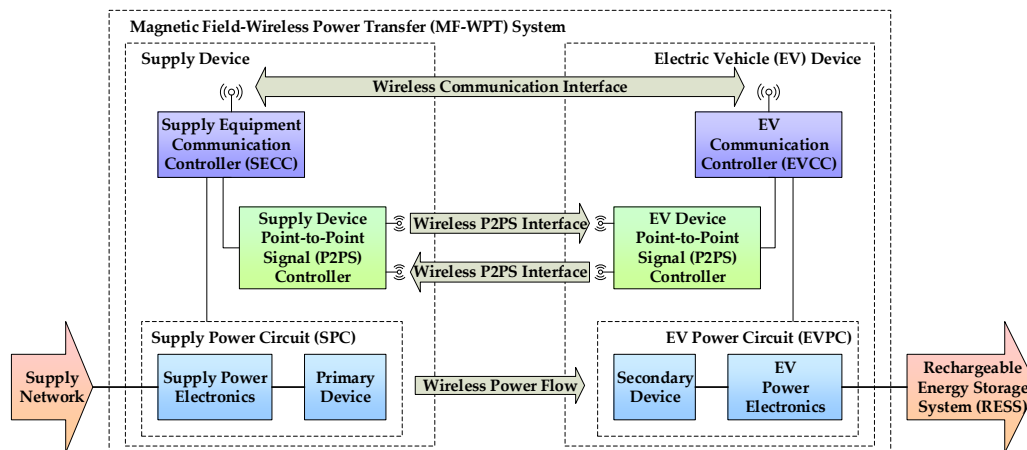
Figure 1. The architecture of an electric vehicle magnetic field wireless power transfer (EV MF-WPT).

First, we describe the supply devices corresponding to the infrastructure. The first sub-system is the supply power circuit (SPC), which generates and transmits magnetic field energy. The SPC can be divided into the components of the supply power electronics and the primary devices. The primary device is a component that receives power from the super network and generates magnetic energy for the WPT (e.g., a primary coil using a Litz wire and ferrite materials). The supply power electronics receives power from the supply network and converts the power and frequency needed by the primary device to WPT (e.g., a power factor correction (PFC), DC-AC inverter, a filter, and an impedance matching circuit). Therefore, the SPC is not only an assembly of components for primary devices and supply power electronics, but also includes electrical and mechanical components. The second sub-system is the supply equipment communication controller (SECC) as the wireless communication interface. The SECC implements wireless communication with the EV communication controller (EVCC) and indirectly interacts with the power transfer process. The last sub-system is the supply device point to point signal (P2PS) controller. The P2PS referred to herein is a unidirectional wireless link between the EV device and the supply device. In other words, the supply device P2PS controller is a component that controls the supply device's P2PS; the main function of this component is alignment (e.g., fine positioning, pairing, and an initial alignment check). The secondary device is aligned in relation to the primary device in the x-, y-, and z-directions to give the secondary device ground clearance. All axial criteria for alignment comply with ISO 4130 [15].

We describe the EV device corresponding to the vehicle relative to the supply device. First, the sub-system of the EV device relative to the SPC of the supply device is the EV power circuit (EVPC). The EVPC is not only an assembly of components for secondary devices and the EV's power electronics, but also includes electrical and mechanical components. The EVPC can be divided into the components of the EV power electronics and a secondary device. The secondary device is a component that receives magnetic energy generated and transmitted by the primary device (e.g., a secondary coil using a Litz wire and a ferrite material). The EV power electronics convert the power and frequency from the secondary device into the DC power output of the EVPC (e.g., the impedance-matching circuit, filter, rectifier, and impedance converter). Second, the sub-system of the EV device related to the SECC of the supply device is the EVCC. The EVCC is an embedded system within the EV that implements wireless communication between the EV and the SECC in order to support specific functions, such as the power transfer and billing process. Finally, the sub-system related to the supply device P2PS controller is the EV device P2PS controller. The EV device P2PS controller is a component that controls the EV device's P2PS, and its main function is alignment.

2.2. ISO 19636, IEC 61980, and SAE J2954: System Requirements

ISO 19363 [14] defines the requirements for the safety and interoperability of an MF-WPT for an EV device. The interoperability addressed by this standard includes the EVPC power classes, secondary device ground clearance range (Z classes), supported frequency range, alignment tolerance area, output power, power transfer efficiency, reference supply power circuit, etc. The safety covered by this standard is electro-magnetic compatibility (EMC), electrical protection, protecting the functionality of active implantable medical devices (AIMDs), etc. Moreover, ISO 19363 describes the test setup and procedure to be applied for conformance testing at the vehicle and component levels.

IEC 61980 [10–12] defines the requirements for the MF-WPT from an infrastructural perspective. These standards consist of three parts. Part 1 [10] addresses the EV WPT's general background, such as operating conditions, electrical safety, and EMC. Part 2 [11] covers the EV MF-WPT's system activities and communication between the EV device and supply device. IEC 61980-2 describes two techniques with fine positioning and pairing methods. One is the low power excitation (LPE) method and the other is the low-frequency (LF) signal method. The LPE energizes the primary device as a P2PS. To be more specific, the LPE uses the existing power transfer coil in the primary device to create a safe yet detectable magnetic field and uses the coil in the secondary device to detect the magnetic field. The LF signal is transmitted from the EV device as a P2PS. To be more specific, the LF signal uses a magnetic field antenna, which uses the LF band in the radio spectrum defined by the International Telecommunication Union (ITU) [16]. The LF magnetic field signal, in its most basic form, consists of a field generation source transmitter and a magnetic receiver that is sensitive to the generated field. We are mainly interested in the fine positioning methods between the primary device and the secondary device using LF magnetic field signals. Part 3 [12] applies to specific requirements for the supply device of the MF-WPT for EV. IEC 61980-3 describes the system infrastructure requirements, constructional requirements, safety requirements, and reference EV power circuit.

SAE J2954 [13] defines the requirements for the alignment methodology, as well as wireless power transfer for light-duty electric and plug-in electric vehicles. This standard covers both EV and infrastructure systems.

2.3. ISO 15118, SAE J2836-6, J2847-6, and J2931-6: Wireless Communication

ISO/IEC 15118 [17–19] addresses the conductive and wireless charging high-level communication (HLC) between the EVCC and SECC. ISO 15118 consists of eight standards, but there are three documents related to WPT. To be more specific, part 1 [17] addresses the requirements of use-cases, part 20 [18] covers the requirements of network and application layer communication messages, and part 8 [19] applies the requirements of the physical layer and data link layer.

Among the SAE standards, J2836-6 [20] addresses the requirements of use-cases for communication between the EV device and the supply device, J2847-6 [21] covers the requirements of communication messages between the EV device and the supply device, and J2931-6 [22] applies the requirements for physical layer and data link layer communication between the EVCC and the SECC.

These six standards refer to the standards in the reference model for seven-layer open system interconnection (OSI) [23]. Other parts of the standards not mentioned above are covered by conductive charging and are not addressed in this paper. Figure 2 shows the relationship between the ISO/IEC standards and the SAE standards for the seven-layer OSI.
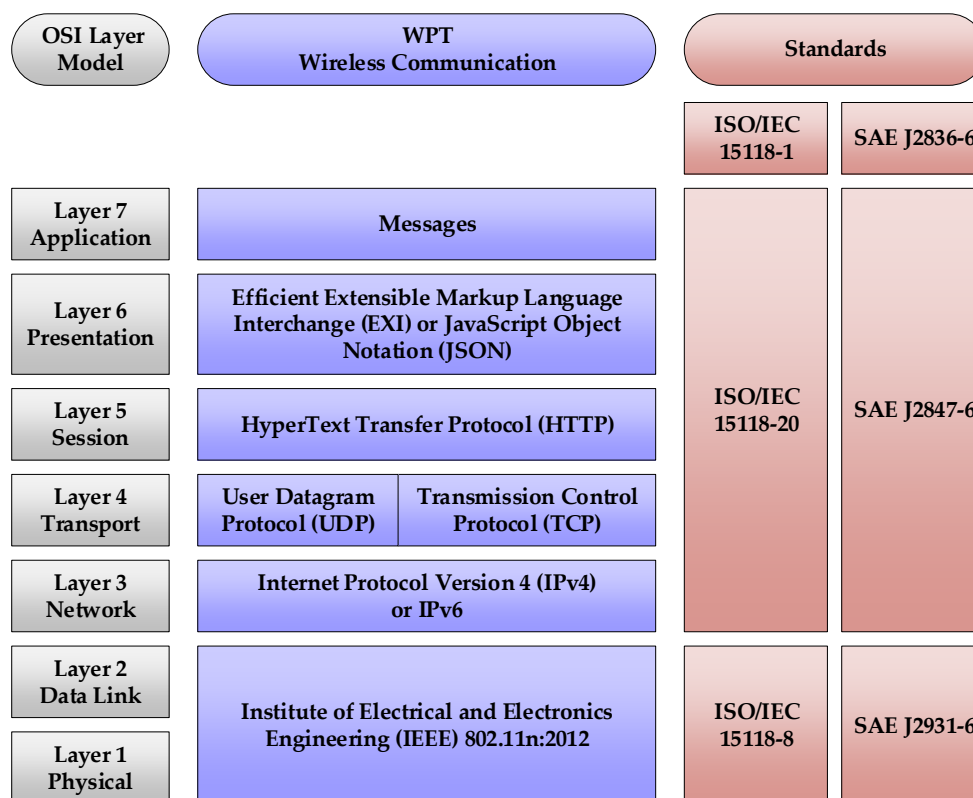
OSI Layer Model	WPT Wireless Communication	Standards	
		ISO/IEC 15118-1	**SAE J2836-6**
Layer 7 Application	**Messages**	**ISO/IEC 15118-20**	**SAE J2847-6**
Layer 6 Presentation	**Efficient Extensible Markup Language Interchange (EXI) or JavaScript Object Notation (JSON)**		
Layer 5 Session	**HyperText Transfer Protocol (HTTP)**		
Layer 4 Transport	**User Datagram Protocol (UDP)** / **Transmission Control Protocol (TCP)**		
Layer 3 Network	**Internet Protocol Version 4 (IPv4) or IPv6**		
Layer 2 Data Link	**Institute of Electrical and Electronics Engineering (IEEE) 802.11n:2012**	**ISO/IEC 15118-8**	**SAE J2931-6**
Layer 1 Physical			

Figure 2. Seven-layer open system interconnection (OSI) of EV MF-WPT high-level communication (HLC).

2.4. IEC 61980-2 and SAE J2954: Alignment Methodology and Positioning Mechanism

IEC61980-2 and SAE J2954 describe two types of alignment methodologies that can maximize the wireless power transfer efficiency between the EV device and the supply device. One is the LPE [13], which directly uses the primary device and the secondary device, and the other is the LF signal [11], which uses an LF-FRA via the auxiliary method. Many indoor and outdoor positioning systems have been developed and applied as standards, including the Global Navigation Satellite System (GNSS), location-based service (LBS), etc. The auto valet parking system (AVPS) has also been developed for vehicles and is being applied as a standard. However, because the positioning accuracy of the alignment method required by the EV MF-WPT will be within 20 mm at a distance of 4.0 m, it is difficult to meet the criteria required by the EV MF-WPT with existing positioning systems. Therefore, using IEC 61980-2 and SAE J2954, we selected the LPE and an LF signal as the alignment methodology most suitable for EV MF-WPT.

The two pertinent methodologies are explained in detail as follows. The LPE uses existing power transfer coils for fine positioning. The primary device is excited at a very low current and does not exceed International Commission on Non-Ionizing Radiation Protection (ICNIRP) 2010 [24] basic restrictions. The EV uses the secondary device to detect the magnetic field generated by the primary device. At this time, the secondary device can only detect the magnetic field from about 0.5 m away. EV uses induced current or voltage to perform the additional functionality of positioning, pairing, and an alignment check. The LF signal is a digitally modulated magnetic field operating at a low frequency, and this signal uses the LF band among the ITU frequency and wavelength bands. The LF signal uses LF-FRA, which is an auxiliary method for fine positioning; the LF-FRA is integrated into both the primary device and the secondary device. "Auxiliary" means that a coil other than a power transfer coil is used for fine positioning. Unlike the LPE, an LF signal allows the primary device or the secondary device to function as a transmitter for fine positioning. If the LF-FRA that transmits the LF signal is integrated into the secondary device, the secondary device functions as a transmitter for fine positioning. The LF signal

receiver can detect the magnetic field from about 4.0 m away and send positional information back to the EV via the wireless communications interface. In the same way as LPE, EV uses the magnetic field generated by the transmitter to also perform positioning, pairing, and an alignment check.

The fine positioning mechanism provides support for the EV or EV driver when it is closer than 4.0 m from the parking spot to establish the central alignment point between the primary device and the secondary device. When it is precisely aligned, the secondary device will be within the defined allowable alignment tolerance area of the primary device. The exact coincidence of the center alignment points of the primary device and the secondary device means that the EV MF-WPT's power transfer efficiency can be maximized. Our positioning system aims to simulate and actually test this LF signal in a parking spot selected by the EV MF-WPT WLAN sequence to determine and confirm the best way to perform fine positioning.

Figure 3 describes the overall EV MF-WPT process. The EV MF-WPT wireless local area network (WLAN) sequence is a process known by WLAN devices: (i) When the EV driver or user connects to the WLAN for EV MF-WPT, the EVCC and the SECC activate the wireless interface for compliance, as defined in ISO 15118-8. If the EV device and the supply device are ready, then (ii) the EV or EV driver will perform fine positioning based on the EV MF-WPT alignment sequence in IEC 61980-2 and SAE J2954. The supply device performs authorization to check whether the EV has finished pairing. The supply device allows charging if an EV, EV driver, or user provides the mechanism for payment: (iii) the EVCC may present a contract certificate and automatically charge; otherwise, the EV driver or a user may present a credit card or a debit card. The supply device will then validate the alignment check: (iv) the secondary device is within the alignment tolerance area, as defined in IEC 61980-3 and ISO 19363. An alignment check will be successfully performed before the MF-WPT. After the supply device alignment check, this device will transfer power between the primary device and the secondary device upon request from the EVCC. Moreover, the supply device will be able to exchange information via wireless communication with the EVCC to perform a power transfer with the EV device.
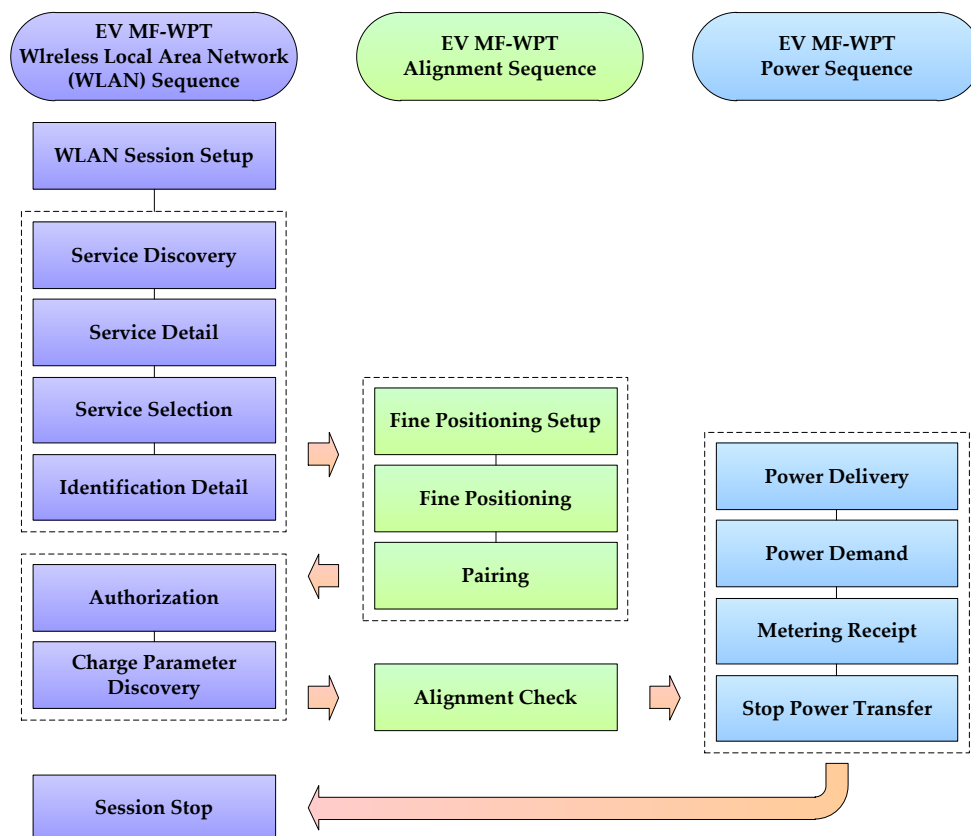

Figure 3. EV MF-WPT charging process.

3. Theoretical Background

In this section, we describe the basic electrical principles of EV MF-WPT and the theoretical background of the LF-FRA. As mentioned before, the purpose of this paper is to present the optimal positioning system simulation and actual test results using our developed LF-FRA.

3.1. The Basic Principle: EV MF-WPT

The classification of WPT technology can be divided into various near-field techniques, such as inductive coupling, magnetic resistance coupling, and capacitive coupling [2]. The technical classification of EV MF-WPT in international standards and regional standards is magnetic resonance coupling [25,26]. The magnetic resonance coupling method is used to compensate the capacitor to improve the system efficiency and capability. Compensation capacitors are used in both SPC and EVPC, and are usually based on four basic electrical circuit topologies [27–30]. These topologies are series to series (SS), series to parallel (SP), parallel to series (PS), and parallel to parallel (PP) compensation. Figure 4 illustrates a circuit diagram of the SPC voltage source (V_1) to the EVPC resistive load (R_L). These four compensation topologies have different advantages. However, there are some issues to consider for these topologies to be applied to EV. As defined by international and regional standards, the operating frequency should be in the range of 79 to 90 kHz, and the nominal frequency should be 85 kHz [13,16]. Moreover, the MF-WPT system should be applied to mass-produced EV, so the total cost should be low [27]. Therefore, this paper considered an SS and SP topology.
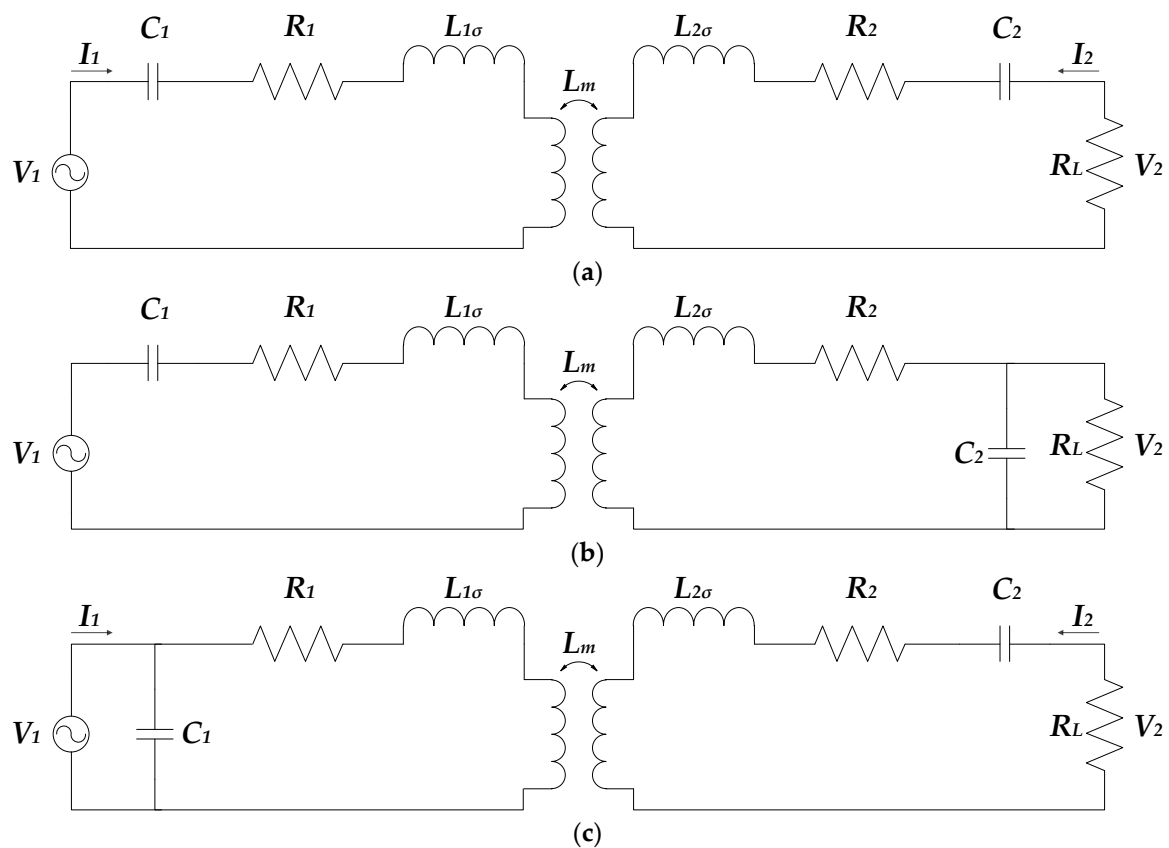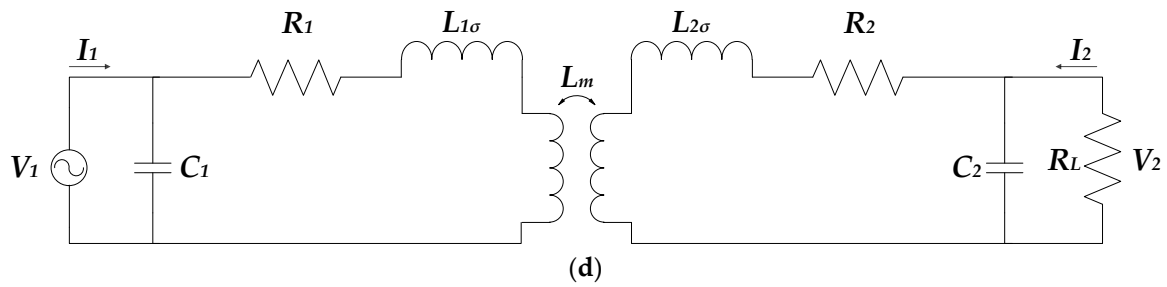
(a)

(b)

(c)

Figure 4. *Cont.*

(d)

Figure 4. Equivalent circuit diagram of WPT compensation topologies: (**a**) series to series (SS) topology, (**b**) series to parallel (SP) topology, (**c**) parallel to series (PS) topology, and (**d**) parallel to parallel PP topology.

The network analysis of the equivalent circuit of SS and SP topology is as follows [27–30]: (i) the impedance (Z_1) of the network by the SPC voltage source of the SS topology is given by:

$$Z_1 = R_1 + j\left(\omega L_1 - \frac{1}{\omega C_1}\right), \tag{1}$$

where R_1 and C_1 are the SPC resistance and capacitor, ω is the SPC sinusoidal voltage source with an oscillation angular frequency, $L_{1\sigma}$ is the leakage inductance of SPC, L_m is the mutual inductance between SPC and EVPC, and L_1 is the self-inductance of SPC. The impedance (Z_2) of the network by the EVPC voltage source of the SS topology is given by:

$$Z_2 = R_2 + R_L + j\left(\omega L_2 - \frac{1}{\omega C_2}\right). \tag{2}$$

The efficiency (η) of the SS topology power transfer is given by:

$$\eta = \frac{P_2}{P_1} = \frac{(\omega L_m)^2 R_L}{Z_2\left[Z_1 Z_2 + (\omega L_m)^2\right]}, \tag{3}$$

where P_1 and P_2 are the power of the SPC and EVPC, respectively. (ii) The Z_1 of the network according to the SPC voltage source of the SP topology is given by:

$$Z_1 = R_1 + j\left(\omega L_1 - \frac{1}{\omega C_1}\right). \tag{4}$$

The Z_2 of the network according to the EVPC voltage source of the SP topology is given by:

$$Z_2 = R_2 + j\omega L_2 + \frac{R_L}{1 + j\omega C_2 R_L}. \tag{5}$$

The η of the SP topology power transfer is given by:

$$\eta = \frac{P_2}{P_1} = \frac{(\omega L_m)^2 R_L}{Z_2\left[Z_1 Z_2 + (\omega L_m)^2\right](1 + j\omega C R_L)^2}. \tag{6}$$

3.2. The Basic Theory: LF-FRA

An antenna is a device that provides a transition from a guided wave on a transmission line to a free-space wave used with a transmitter or receiver [31]. There are a wide variety of antenna types and geometries. A ferrite rod antenna is classified as an electrically small loop antenna [31]. This is the simplest structure, and an electrically small air core loop antenna is usually classified as electrically

small $\lambda/2\pi < 0.16\ \lambda$ [32,33]. An antenna volume can be physically bounded by a sphere with a radius equal to $\lambda/2\pi$. The electrically small air core loop of a single turn has very low radiation resistance. In other words, the general description of the electrical air-core small loop antennas involves the size of the antenna being very small compared to the wavelength; in this way, the radiation resistance (R_r) of the antenna becomes very small, and its reactance becomes relatively large. Moreover, the radiation efficiency (RE) can be reduced, as given by [32]:

$$\text{RE} = \frac{R_r}{R_r + R_L} \ll 1, \tag{7}$$

where R_r is radiation resistance and R_L is loss resistance. The output voltage across the loop terminals and R_r is given by [32]:

$$V = \frac{2\pi AEQ\cos\theta}{\lambda}, \tag{8a}$$

$$R_r = \frac{\eta 8\pi^3 A^2}{3\lambda^4}, \tag{8b}$$

where A is the area of the loop in square meters, E is the radio frequency (RF) field strength in volts per meter, Q is the loaded charge of the tuned circuit, θ is the angle between the plane of the loop and the signal source, λ is the wavelength of the operation in meters, and η is the impedance of free space. If the air core loop antenna has N turns, then the output voltage across the loop terminals and R_r increases with a factor of N^2 and is given by [32]:

$$V = \frac{2\pi ANEQ\cos\theta}{\lambda}, \tag{9a}$$

$$R_r = \frac{\eta 8\pi^3 A^2 N^2}{3\lambda^4}, \tag{9b}$$

where N is the number of turns in the loop.

In a ferrite rod antenna, the wire is wound around the ferrite rod to form a coil. Both the multi-turn coil and the increased relative permeability inside the coil increase the voltage that can be induced in the antenna by an incident electromagnetic field. The R_r and RE can be raised by inserting a ferrite rod, which has a high magnetic permeability in the operating frequency band. In other words, a large magnetic flux is required to obtain a large induced voltage, and this is the basis for high magnetic permeability. The magnetic properties of a ferrite rod depend not only on the relative magnetic permeability μ_{rod} of its material, but also on its geometry. The radiation resistance of a ferrite rod (R_{rod}) is μ^2_{rod} times larger than an R_r of the same geometry. Therefore, if the ferrite rod loop antenna has N turns, then the output voltage across the ferrite rod loop terminals and R_{rod} increases with a factor of μ_{rod} and is given by [32]:

$$V_{rod} = \frac{2\pi ANEQ\mu_{rod}}{\lambda}, \tag{10a}$$

$$R_{rod} = \frac{\eta_0 8\pi^3 A^2 N^2 \mu^2_{rod}}{3\lambda^4}, \tag{10b}$$

where μ_{rod} is the corrected ferrite rod permeability.

Figure 5 shows a typical series resonant equivalent circuit diagram of the LF-FRA. The LF-FRA is made of a ferrite rod around which a coil is wound. The LF-FRA can be modeled as an inductor that has various resistances in series due to antenna losses. The total impedance (Z_{total}) of an LRC circuit [34] is given by:

$$Z_{total} = R + j(X_L + X_C), \tag{11}$$

where X_L is the inductive reactance, and X_C is the capacitive reactance. The LF-FRA impedance needs to be matched to the input impedance of the rest of the circuit. At the specific frequency where

$X_L = -X_C$, the imaginary components of the impedance exactly cancel each other out. At this frequency, the impedance of the circuit has the smallest magnitude and a phase angle of zero. This is called the resonance frequency (f_0) of the circuit [34] and is given by:

$$f_0 = \frac{1}{\sqrt{LC}} = \omega_0 \tag{12}$$

where ω_0 ($2\pi f_0$) is the resonant angular frequency. In an electrical resonator, circuit damping is caused by the loss of energy in resistive components. The quality factor (*Q*-factor) is can be described as [34]:

$$Q(w) = \omega \frac{\text{Maximum Energy Stored}}{\text{Power Loss}} \tag{13}$$

where the *Q* factor depends on the frequency. At the resonant frequency, the maximum energy stored in a resonant circuit can be calculated from the max energy stored in the inductor. Real power [34] is only dissipated in the resistors and is given by:

$$P = V_{Rrms} \times I_{Rrms} = I_{Rrms}^2 R = \frac{V_{Rrms}^2}{R}, \tag{14}$$

where V_{Rrms} is the root mean square (rms) voltage through the resistor, and I_{Rrms} is the rms current through the resistor. For the series resonance circuit, *Q* is the easiest-to-consider current [34] and is given by:

$$Q = \frac{\omega_0 L}{R} = \frac{1}{\omega_0 RC} \tag{15}$$

which shows that *Q* increases as *R* decreases. The width of the resonance peak is a useful measure of the frequency selectivity of the resonant circuit. The bandwidth (B) of the resonant circuit is defined as the difference between f_2 and f_1, which is a frequency 3 dB lower than the resonant frequency. One of the most efficient methods for driving the resonant circuit is a switching amplifier in either a full or half-bridge mode. A half-bridge offers very good results as it has the advantage of being low cost and easy to implement [35]. Figure 6 shows a half-bridge drive circuit for the LF-FRA.
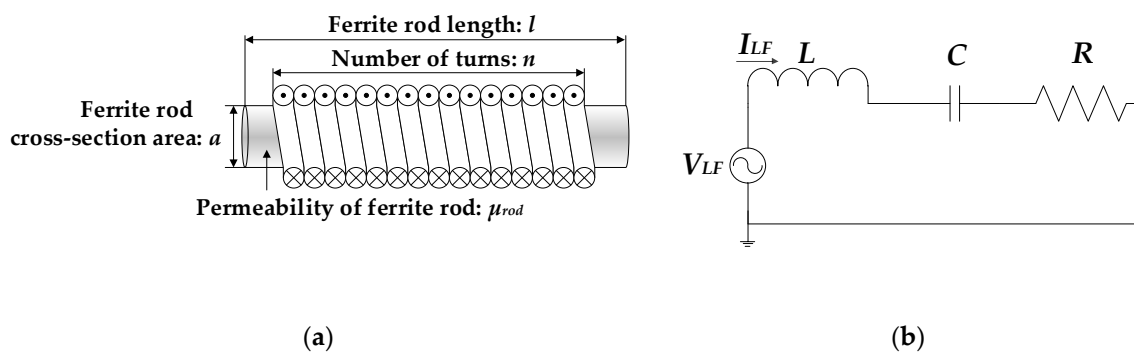

(**a**)　　　　　　　　　　　　　　　　　　　　　　　　(**b**)

Figure 5. Equivalent circuit diagram of low-frequency ferrite rod antenna (LF-FRA): (**a**) the geometrical dimension of the LF-FRA and (**b**) the equivalent circuit of the LF-FRA.
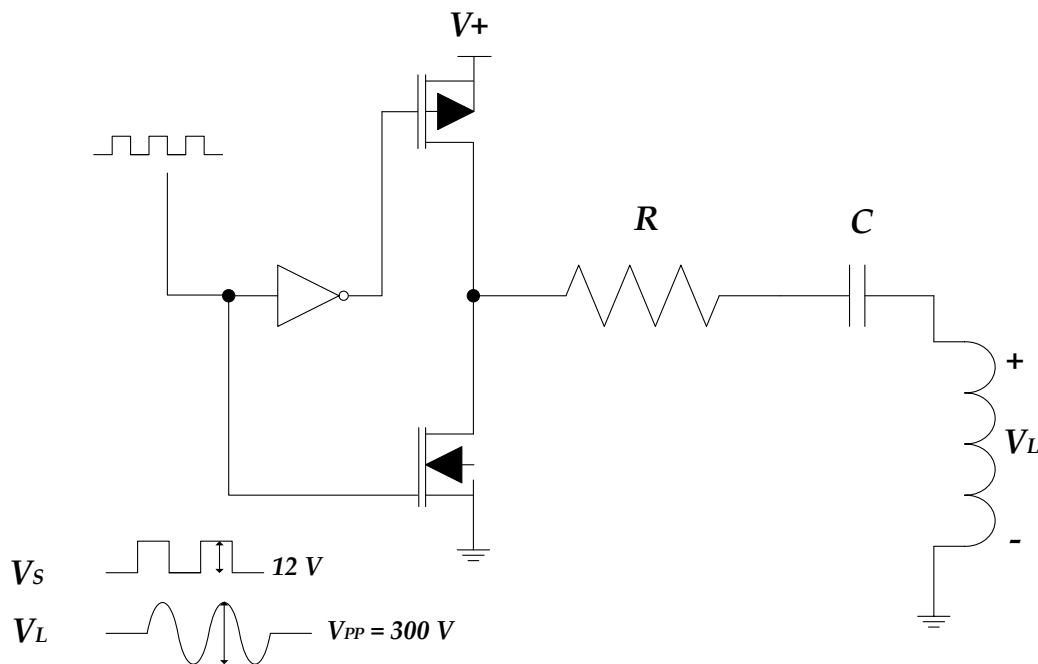
Figure 6. The half-bridge drive circuit for the LF-FRA.

Additionally, some of the main advantages of using a magnetic field antenna, such as the LF-FRA, are as follows. First, an RF electromagnetic wave antenna is susceptible to scattering and distortion. However, a magnetic field antenna is less prone to distortion and can penetrate non-magnetic materials, such as water, plastic, etc. Second, a magnetic field attenuates much more rapidly, so it is easy to precisely control the range. Finally, the LF-FRA can be built in smaller sizes and can be used for a variety of purposes due to its lower cost of production. This also briefly explains the simulation and modeling of the LF-FRA for its application in fine positioning.

3.3. Basic Technology: Positioning

Triangulation is the classic method used to determine position. There is also a received signal strength indicator (RSSI), which is a method for determining position using the strength of a communication signal as communication technology develops [36].

Triangulation is the most common method used to estimate the real-time position of an object moving in a two-dimensional plane. At least three reference points are required to estimate the real-time position of an object moving in a two-dimensional plane. If these reference points are referred to as P_1, P_2, and P_3, with the moving object represented as M, the present position is (x, y) and the distance from the moving object M to the three reference points is d_1, d_2, and d_3; then, the distance between each reference point from moving object M can be simply calculated using the Pythagorean theorem. The distance between each reference point is given by:

$$d_1^2 = (x - x_1)^2 + (y - y_1)^2, \tag{16a}$$

$$d_2^2 = (x - x_2)^2 + (y - y_2)^2, \tag{16b}$$

$$d_3^2 = (x - x_3)^2 + (y - y_3)^2. \tag{16c}$$

Second, RSSI is a method for measuring the distance between a transmitter and a receiver using the path loss of radio waves. The basic principle of RSSI is based on triangulation. The distance

between the moving object and the reference point uses the Friis equation. The difference between the transmitted and received signal strength is given by:

$$P_{Tx} - P_{Rx} = 20 log_{10}\left(\frac{4\pi d}{\lambda}\right), \tag{17}$$

where P_{Tx} is the transmitted signal strength, P_{Rx} is the received signal strength, λ is the wavelength, and d is the distance between two points. The distance between two points is given by:

$$d = \frac{\lambda}{4\pi} 10^{\frac{P_{Tx}-P_{Rx}}{20}} = \frac{c}{4\pi f} 10^{\frac{P_{Tx}-P_{Rx}}{20}}, \tag{18}$$

where f is the frequency and c is the speed of light. The positioning technology that is intended to be applied to the fine positioning of the EV MF-WPT using the LF-FRA includes a combination of triangulation and RSSI.

4. Pre-Condition

An electrical schematic for the EV MF-WPT system was built with simulation software widely used in industry and academia. We used Maxwell 3D and Simplorer from the ANSYS software package [37] and FEKO from the Altair software package [38]. Maxwell 3D is based on electromagnetic field simulations using finite element analysis (FEA); its main functions are the analysis of electro-static, magneto-static, eddy current, transient electric, and transient magnetic effects. Simplorer can simulate the interactions between electronic components, power electric circuits, and electromechanical controls. The method of moments (MoM)/finite element method (FEM) in FEKO supports a wide spectrum of numerical methods and hybridizations, each being suitable to a specific range of applications. In this section, we briefly describe the EV MF-WPT system, which is the target of our positioning system using the LF-FRA.

4.1. EV MF-WPT System

As shown in Figure 7, we have experience in developing electrical circuits with a class of output power levels up to 7.7 kVA for supply devices and a class with input power levels up to 3.7 kVA for EV devices [39]. The supply network input voltage of this system was single phase 220 V AC, the primary device inductance (GA: src to GA: snk) was 226.72 μH, the secondary device inductance (VA: src to VA: snk) was 225.84 μH, the coupling factor (κ) was 0.08, and the operating frequency was 85 kHz. The primary device and the secondary device tuning capacitor (C18, C1) was 14.55 nF. The geometrical dimensions of the primary device and the secondary device are shown in Figure 8. Detailed parameters for the magnetic field analysis of the primary device and the secondary device are given in Table 1. The magnetic gap [13] between the primary device and the secondary device was 160 mm. As mentioned earlier, a magnetic gap of 160 mm corresponded to the Z2 class in the secondary device ground clearance.
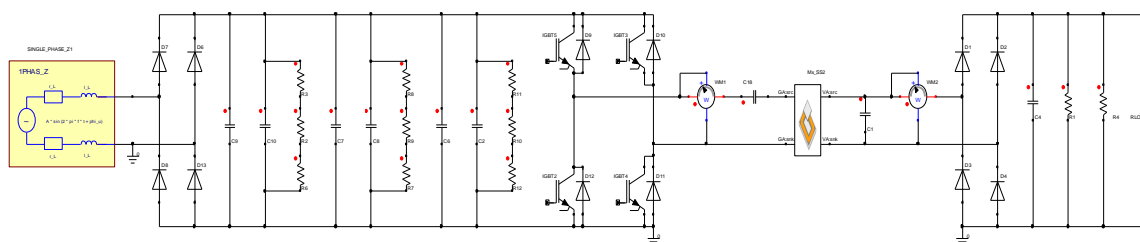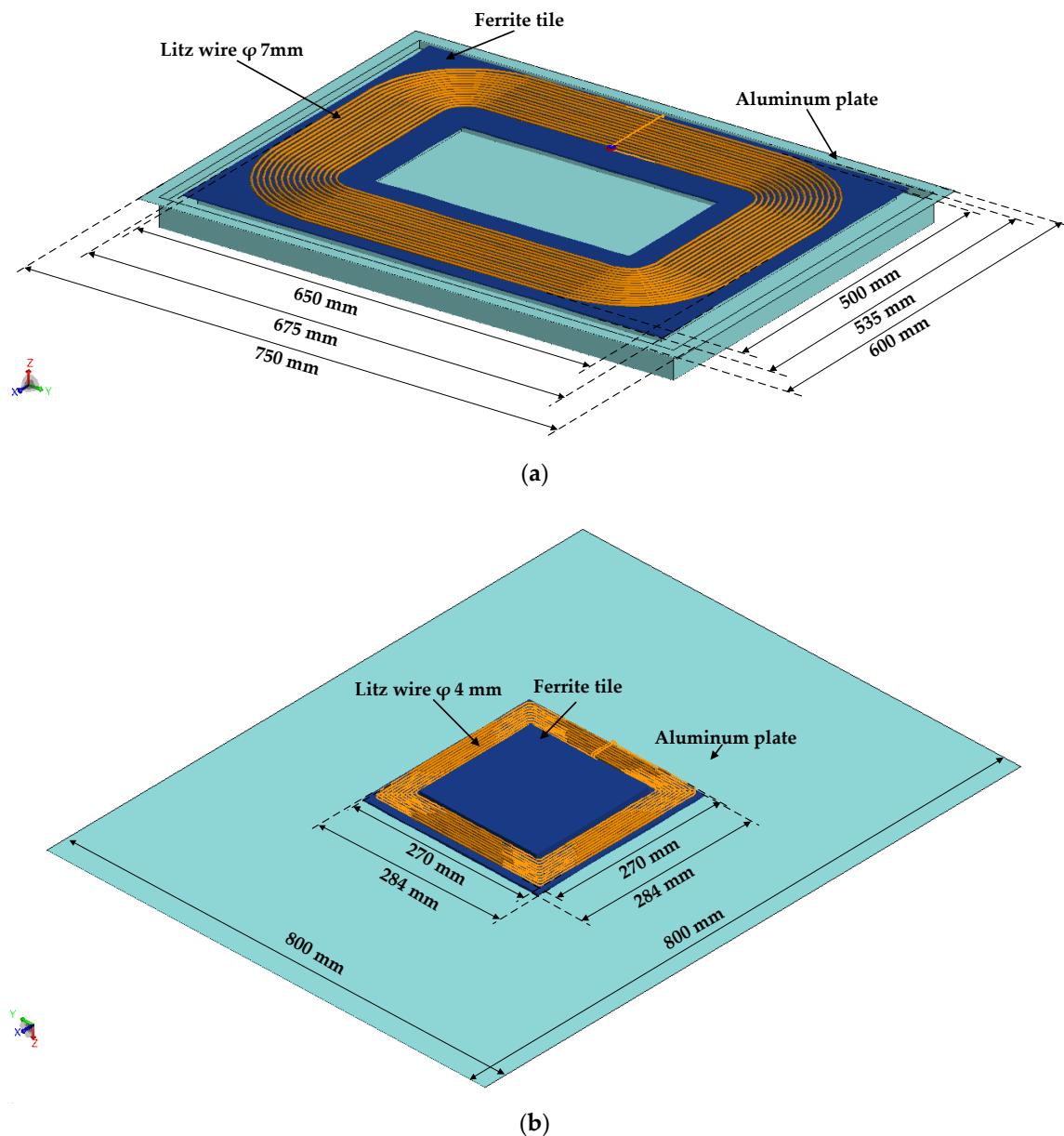

Figure 7. The electrical circuit of the EV MF-WPT.

(**a**)

(**b**)

Figure 8. The geometrical dimensions: (**a**) the primary device's geometrical dimensions and (**b**) the secondary device's geometrical dimensions.

Table 1. Parameters for the magnetic field analysis of the primary device and the secondary device.

Parameter	Primary Device	Secondary Device
Coil material	Litz wire φ 7 mm	Litz wire φ 4 mm
Number of turns	15 turns of single-layer	8 turns of double-layer
Tile material	Ferrite	Ferrite
Shield plate	Aluminum	Aluminum

The circuit simulation results of the input voltage and the current of the supply network using PFC and an inverter reached 155 V AC and 42 A. Then, the output voltage and current passing through the power transfer coil and the compensation circuits was 10 V AC and 3.5 A, respectively, as shown in Figure 9. When the energy was transferred between the primary device and the secondary device, the result of the magnetic field simulations went up to 30 kA/m for the primary device and 8 kA/m for

the secondary device. The value of the magnetic field between the primary device and the secondary device reached as high as 1.35 kA/m, as shown in Figure 10.

(**a**)

(**b**)
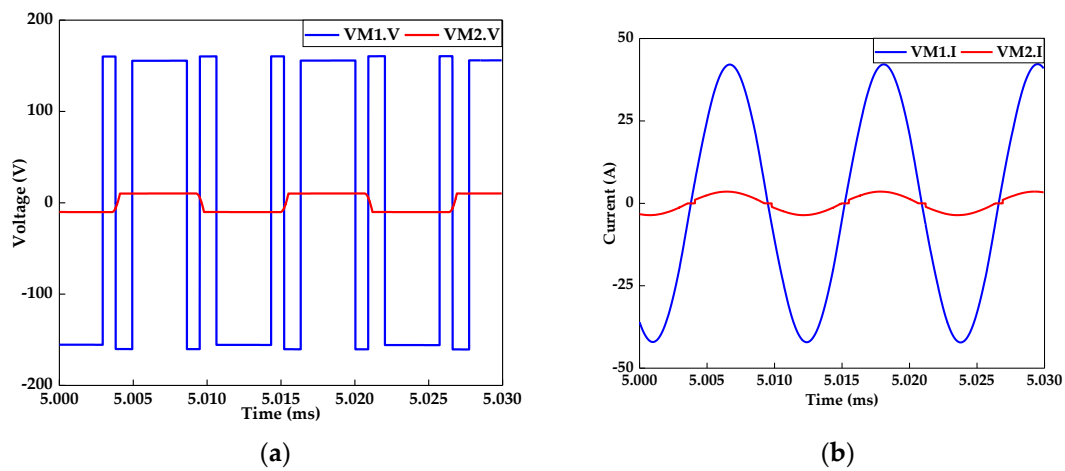
Figure 9. The electrical circuit simulation result of the EV MF-WPT: (**a**) input and output voltage, and (**b**) input and output current.
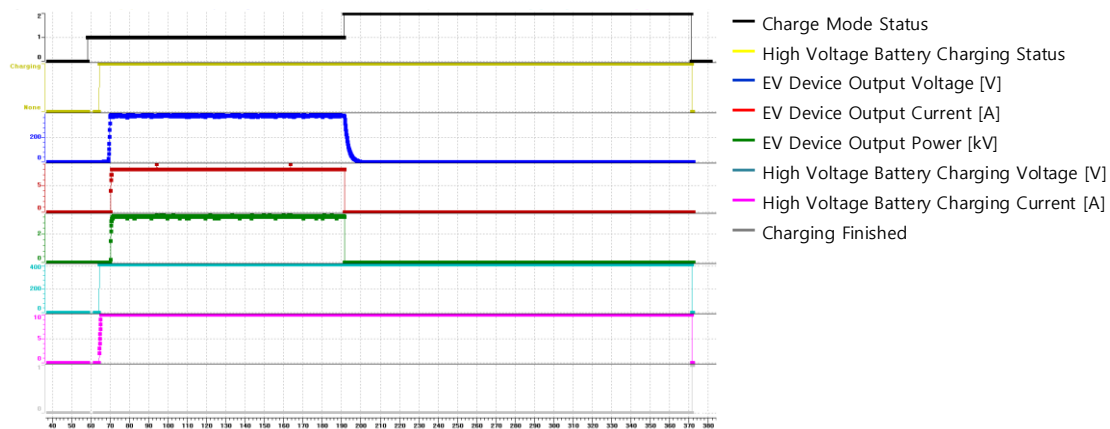

(**a**)

(**b**)

Figure 10. *Cont.*

(c)

Figure 10. The result of the H-field: (**a**) YZ-plane view, (**b**) H-field of the primary device, and (**c**) H-field of the secondary device.

Based on this result, we integrated a supply device with a 7.7 kVA output power level class and an EV device with a 3.7 kVA input power level class into a KIA SOUL EV, as shown in Figure 11. In order to verify the accuracy and feasibility of the simulation results, we measured whether the output power of the EV device correctly supplied power to the high voltage battery of the EV. The measuring instrument used CANoe from the VECTOR software [40], which can check the internal communication of the EV. Figure 12 shows the EV device's output voltage, current, power, and charging voltage, as well as the current of the high voltage battery of the MF-WPT system integrated into the KIA SOUL EV. While the EV was charging wirelessly, the output voltage, current, and power of the EV device were 392 V DC, 9 A, and 3.4 kW, and the charging voltage and current of the high voltage battery were 412 V DC and 100 A.

(a)

(b)

Figure 11. Integration of the MF-WPT in a SOUL EV: (**a**) SOUL EV MF-WPT and (**b**) EV bottom view.

Figure 12. EV device output value of the MF-WPT system in a KIA SOUL EV.

4.2. LF-FRA Simulation Model

Important factors to be considered in LF-FRA modeling used for the fine positioning of an EV MF-WPT are the quality factor (Q-factor), operating frequency, and magnetic field strength (H-field). There is no doubt that it is important to design and model antenna while considering the Q-factor. The reason for considering the operating frequency and H-field in LF-FRA modeling is that these factors should be applied to the vehicle. Since it is an assemblage of many components, the vehicle must comply with the international standards for its operating frequency and radiated power to prevent malfunction and human damage from electromagnetic waves. Also, because the LF-FRA is a new component, it should not malfunction due to interference with existing vehicle components. Therefore, the available operating frequency band of the LF-FRA for the fine positioning of the EV MF-WPT is from 105 kHz to 205 kHz among the LF bands. The H-field recommended by the ITU in this frequency band should not exceed 66 dBμA/m at a distance of 10 m [41].

Based on these important factors, we designed the LF-FRA with an operating frequency of 125 kHz and a bandwidth (BW) of 10 kHz. Here, the resistance was 3.3 Ω, the capacitance was 4.9 nF, and the Q-factor was 84. Figure 13 shows the magnitude and phase of the input impedance of the LF-FRA with an operating frequency of 125 kHz. The magnitude was 10.4 dB, and the phase was 7.5 degrees. Table 2 shows the detailed parameters of the LF-FRA with different operating frequencies.

(**a**)

(**b**)
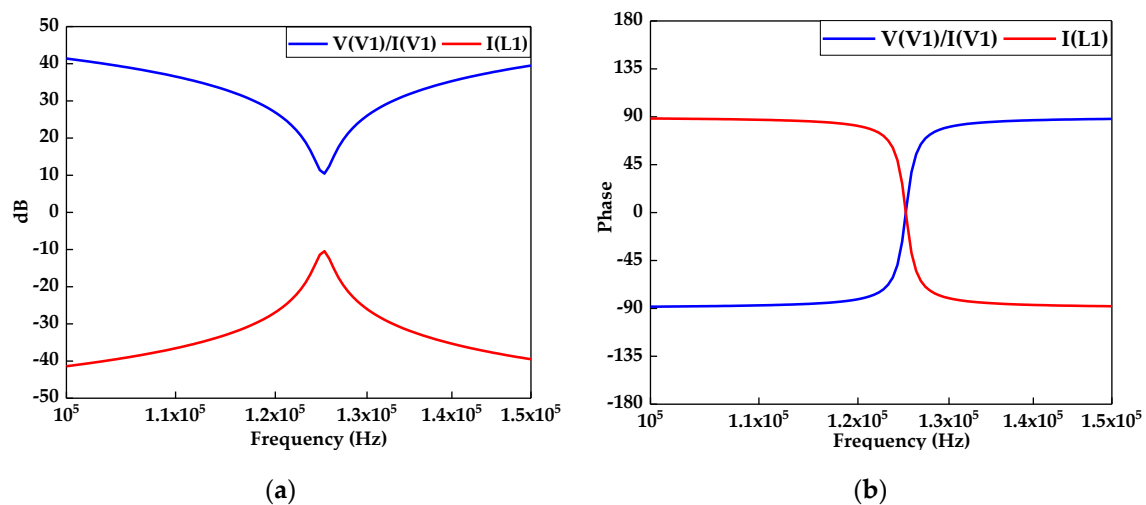
Figure 13. The input impedance of the LF-FRA at 125 kHz: (**a**) the magnitude of the input impedance and (**b**) the phase of the input impedance.

Table 2. LF-FRA parameters by operating frequency.

Operating Frequency (with BW 10 kHz)	Capacitance	Q-Factor
105 kHz	6.96 nF	66
145 kHz	3.65 nF	91
165 kHz	2.85 nF	103
185 kHz	2.24 nF	116
205 kHz	1.83 nF	128

Since the LF-FRA will be mounted on the primary device and the secondary device, the length or thickness of the LF-FRA should be limited to 10 mm. We analyzed the patterns of the near field magnetic flux density (B-field) of three types of LF-FRA using the FEKO software while considering the important factors mentioned above. The geometric dimensions and the results of the simulation of the LF-FRA are shown in Figures 14 and 15. The LF-FRA with a 90-mm width had 70 turns (see Figure 14a), the LF-FRA winding in one direction with a 2.5 mm thickness had 91 turns (see Figure 14b), and the LF-FRA winding in three directions had a total of 491 turns (see Figure 14c). The blue area shown in Figure 15 represents a parking lot with a width of 2 m and a length of 6 m. The geometrical center of the primary device was 2 m away from the inner line of the front of the parking space. The primary device was located on the centerline of the parking space. SAE J2954 [13] mentions the geometrical center position of the primary device installed in the parking lot and the size of the parking lot. Therefore, our simulations also referred to this. From the pattern of the near-field B-field, when the B-field was 4 nT, the LF-FRA with a 90 mm width had a B-field distance a total of 2.70 m from the ±x-direction (see Figure 15a). Importantly, the LF-FRA acting as the receiver did not recognize all the B-fields of the LF-FRA acting as the transmitter, but rather only the B-field in the −x-direction, which is the direction in which the vehicle moves forward. In other words, the recognition distance of the B-field used for the fine positioning was the distance from the geometrical center of the primary device to the B-field formed by the x-direction and the secondary device to the B-field formed by the −x-direction. The minimum B-field value recognized by an LF-FRA acting as a receiver was 4 nT. Table 3 summarizes the distance values of the B-field when the B-field of the other LF-FRAs was 4 nT. In the case of B-field changes due to the operating frequency, the LF-FRA with a 90-mm width did not change, but the other LF-FRA changed. Therefore, the LF-FRA for the fine positioning of EV MF-WPT confirmed that the LF-FRA with a 90-mm width was the optimum condition.

(**a**)

Figure 14. *Cont.*

Copper Wire

Ferrite Rod

Width: 10 mm

Length: 10 mm

Thickness: 2.5 mm
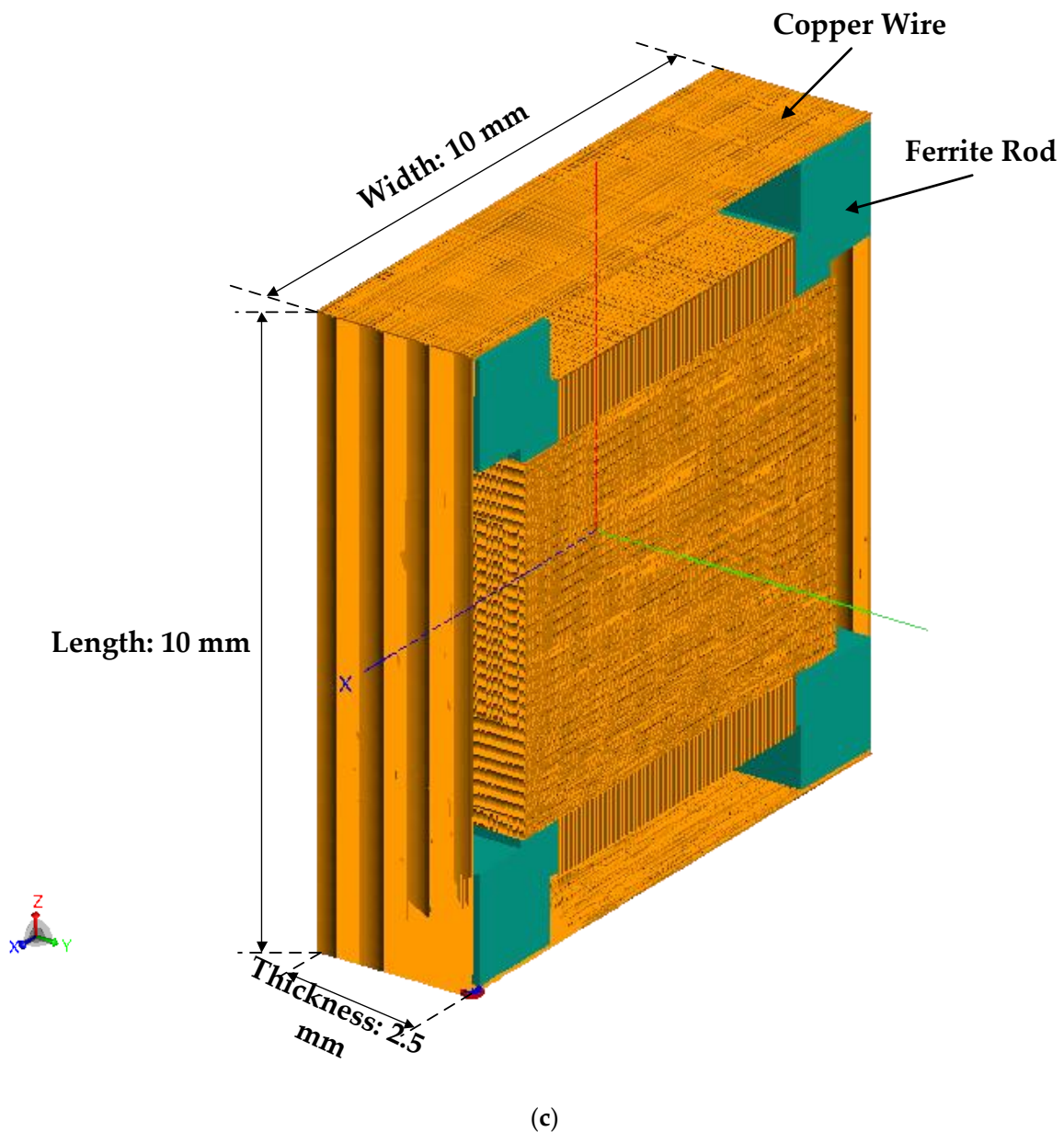
(**b**)

Figure 14. *Cont.*

(**c**)
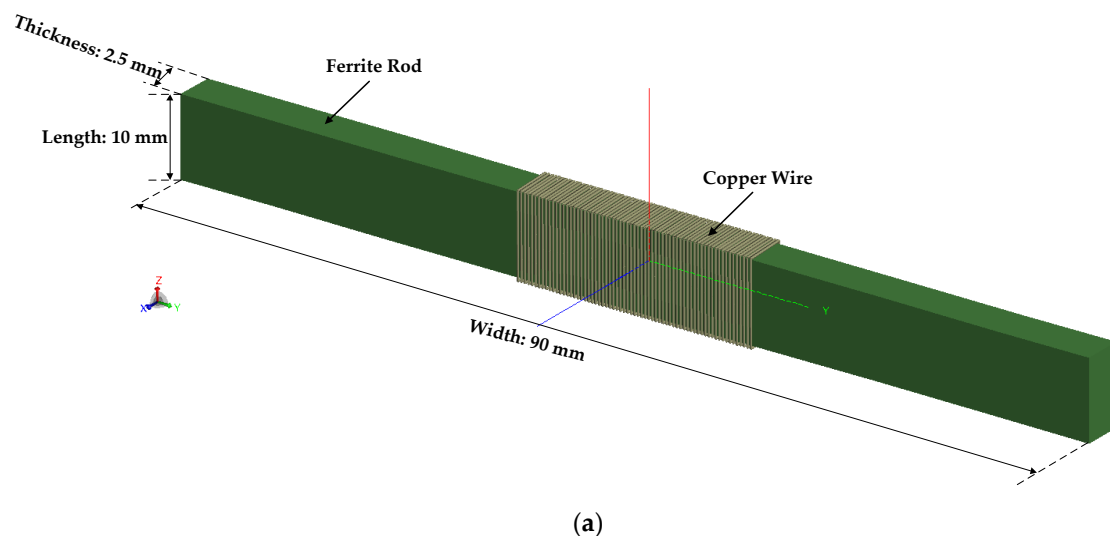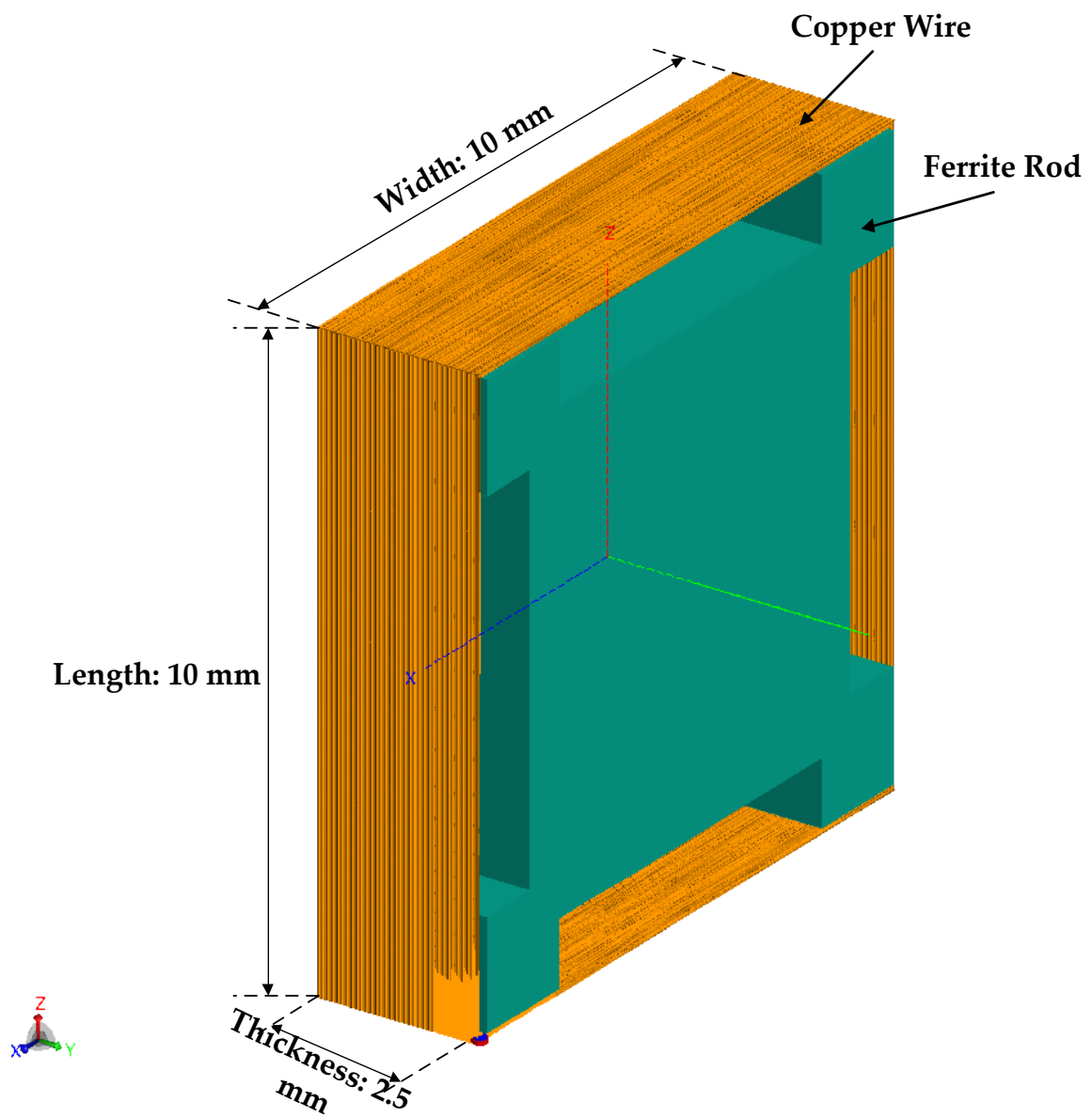
Figure 14. The geometrical dimension of the LF-FRA: (**a**) the LF-FRA with a 90-mm width, (**b**) the LF-FRA winding in one direction with a 10-mm width, and (**c**) the LF-FRA winding in three directions with a 10-mm width.

Table 3. B-field distance value for 4 nT.

Type of LF-FRA	Number of Turns	Total B-Field Distance [1]
1D winding 90-mm width	70	2.70 m
1D winding 10-mm width	91	1.98 m
3D winding 10-mm width	200 (width), 200 (length), 91 (thickness)	1.65 m

[1] ±x-direction.

(**a**)

(**b**)

(**c**)
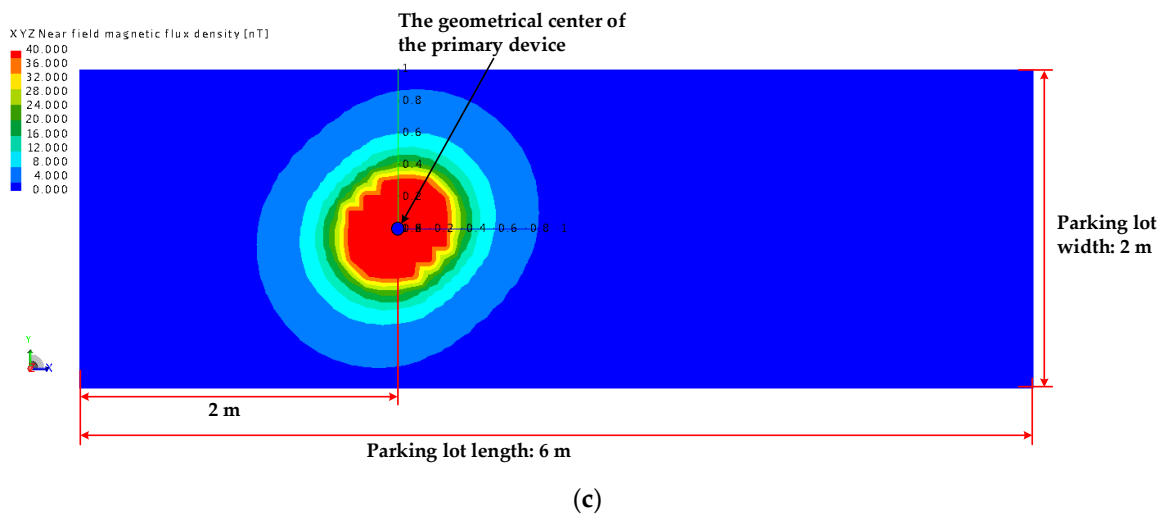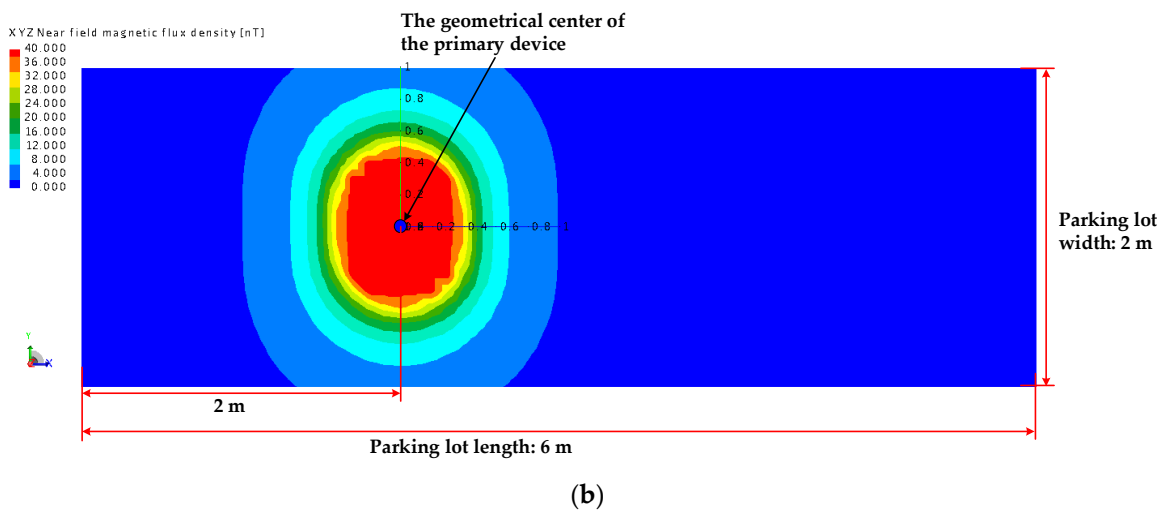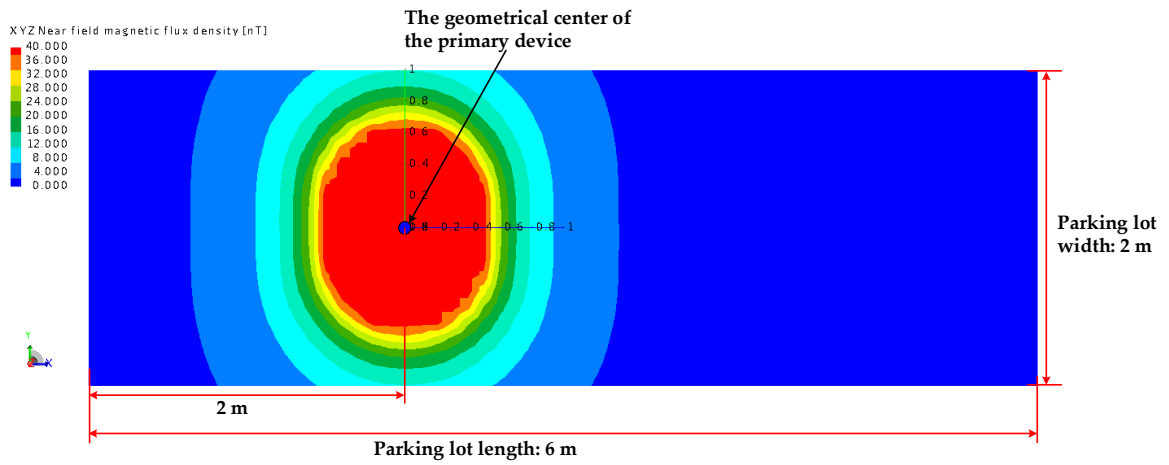
Figure 15. *Cont.*
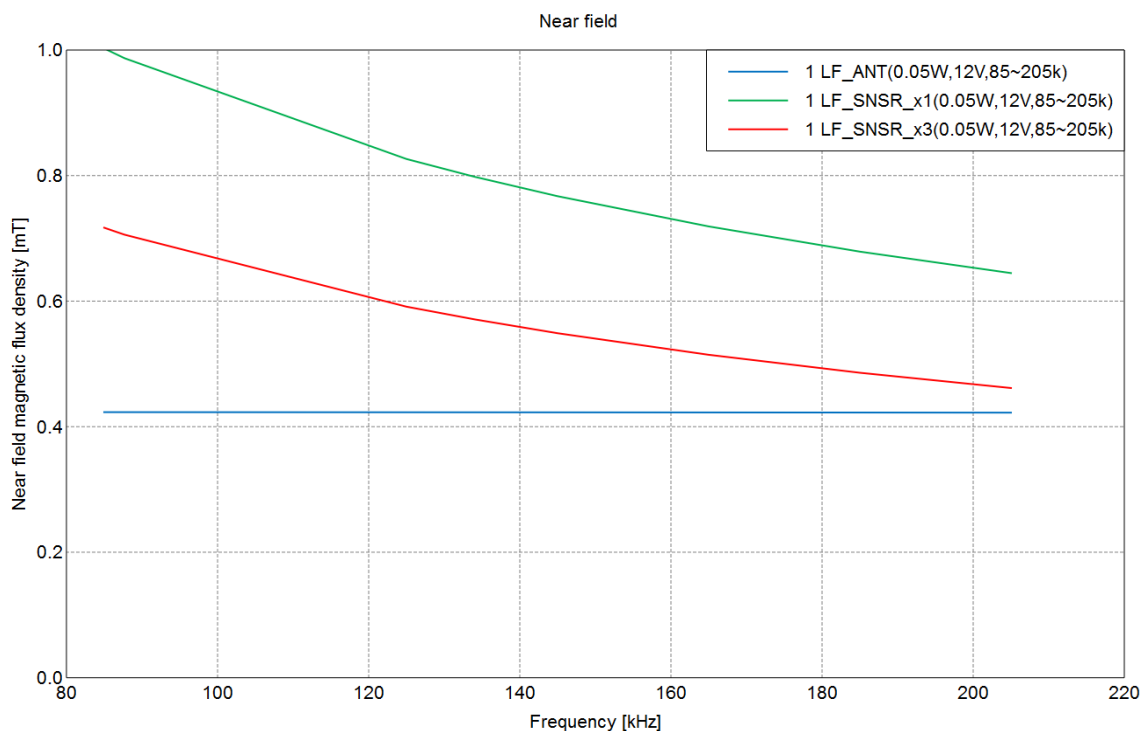
(d)

Figure 15. The pattern of the near-field B-field: (**a**) the LF-FRA with a 90-mm width, (**b**) the LF-FRA winding in one direction with a 10-mm width, (**c**) the LF-FRA winding in three directions with a 10-mm width, and (**d**) B-field changes due to the operating frequency.

5. Simulation

In this section, we optimize the LF-FRA such that the LF-FRA was installed in the power class of all EV MF-WPTs. We attached the primary device and the secondary device to the optimized LF-FRA to determine a positioning method using the B-field. For this purpose, a B-field simulation was performed.

5.1. Optimization of the LF-FRA

As mentioned before, the LF-FRA with a width of 90 mm did not change the B-field even when the operating frequency was changed. Therefore, we optimized this LF-FRA using the FEKO software. The width of the ferrite rod was reduced by 20 mm, and the number of turns was increased, but the LF-FRA was designed such that the characteristics of the B-field were not changed. There were two possible cases in which the LF-FRA can be optimized. The first included a ferrite rod with a width of 70 mm and a number of turns of 120. The second included a ferrite rod with a width of 50 mm and a number of turns of 200. Figure 16 shows the geometric dimensions of the optimized LF-FRA. The results of the B-field simulation of the optimized LF-FRA show that the B-field did not change while the operating frequency changed from 85 kHz to 205 kHz. In addition, while the geometrical center position of the primary device changed from −2 m to 4 m in the x-direction of the parking lot, the B-field demonstrated that the LF-FRA with a width of 50 mm matched the LF-FRA with a width of 70 mm. The same result was confirmed in the y-direction of the parking lot, as shown in Figure 17. Based on this result, the optimum LF-FRA for the fine positioning of the EV MF-WPT had a width of 50 mm, a length of 10 mm, a thickness of 2.5 mm, and 200 turns.
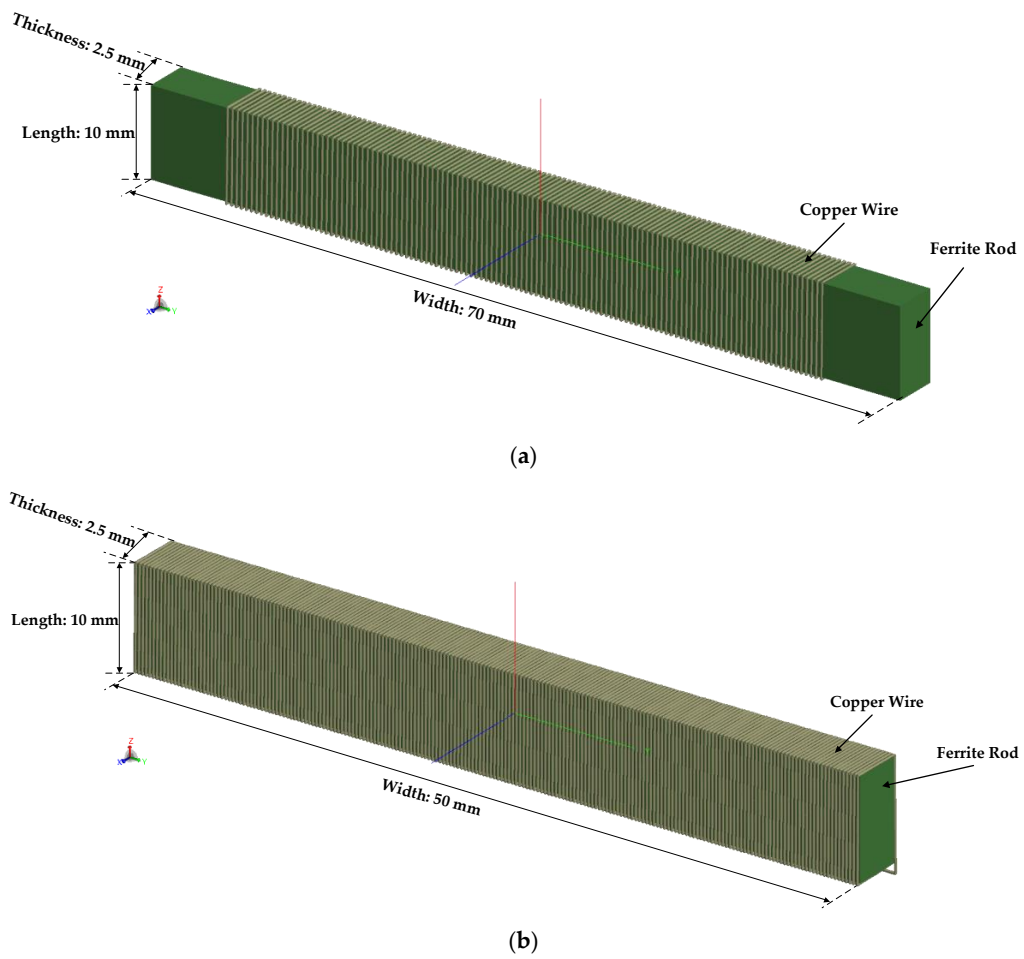
(**a**)

(**b**)

Figure 16. The geometrical dimension of the LF-FRA: (**a**) the LF-FRA with a 70-mm width and 120 turns, and (**b**) the LF-FRA with a 50-mm width and 200 turns.
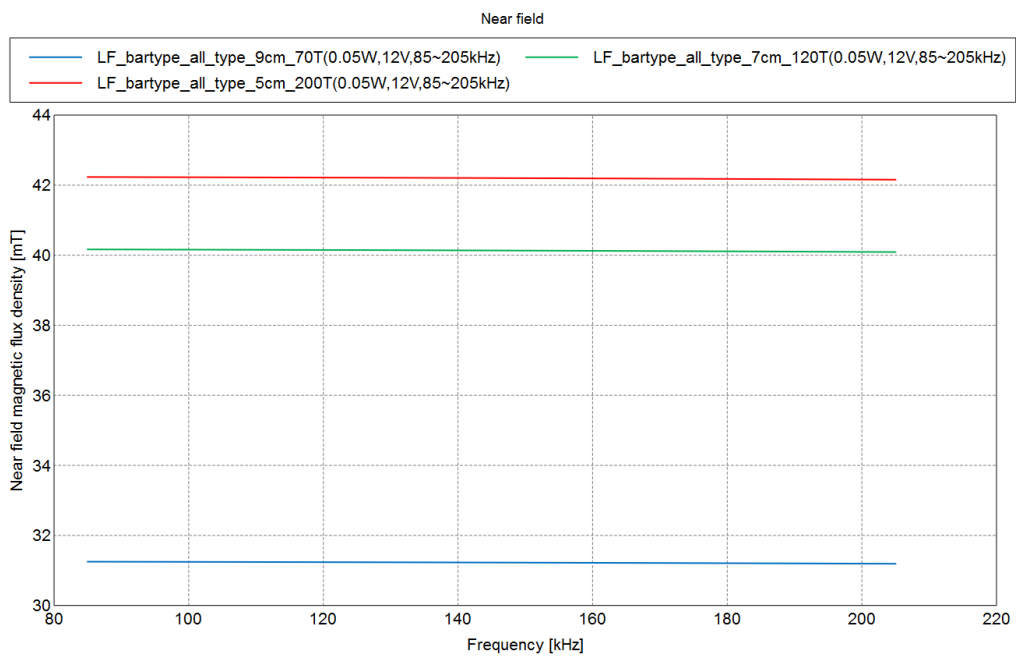
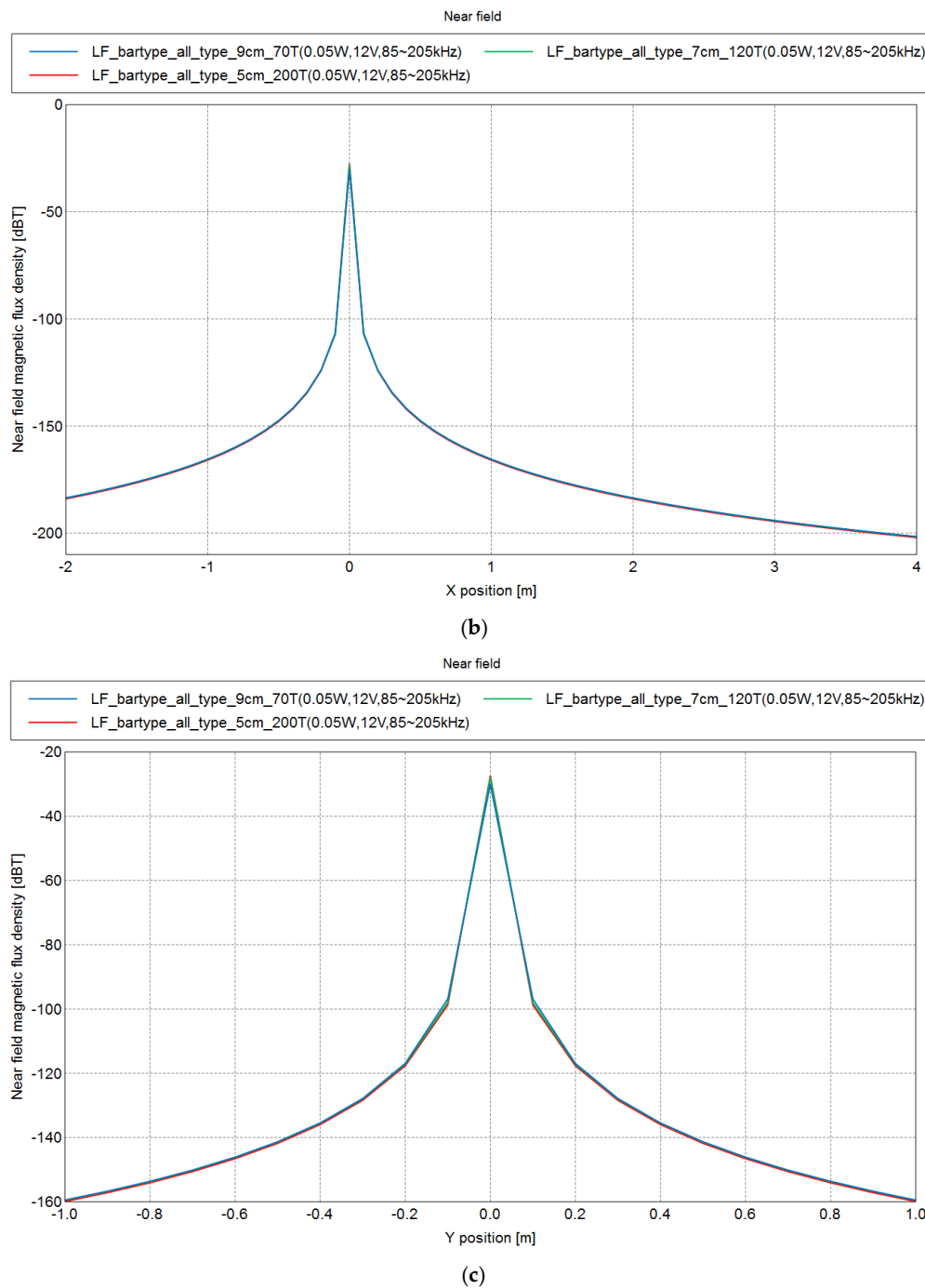

(**a**)

Figure 17. *Cont.*

(b)

(c)

Figure 17. The results of the optimized LF-FRA: (**a**) the B-field changes according to the operating frequency, (**b**) the B-field of the primary device changed from −2 m to 4 m in the x-direction of the parking lot, and (**c**) the B-field of the primary device changed from −1 m to 1 m in the y-direction of the parking lot.

5.2. LF-FRA Fine Positioning

In order to estimate the real-time position of an object moving in a two-dimensional plane, at least three reference points are required. Estimating the location between the primary device and the secondary device requires at least four reference points because they are three-dimensional planes. In addition, the LF-FRA integrated into the secondary device installed only the minimum number of LF-FRAs since interference with the other electronic components of the vehicle should not occur.

Since the primary device is fixed in the parking lot, there are two ways to place the LF-FRA on the primary device. One arranges the LF-FRA at each corner of the primary device, and the other arranges

the LF-FRA at the center of each side of the primary device. Because the EV moves and finds the primary device, there is only one method used to place the LF-FRA into the secondary device, and only two LF-FRAs are used. In other words, the LF-FRA is arranged at the center of each side of the secondary device. There is also a direction in which the primary device generates a magnetic field and transfers energy to the secondary device. Therefore, when the LF-FRA was placed in the primary device and the secondary device, it was placed according to the direction of the magnetic field. Figure 18 shows the LF-FRAs arranged on the primary device and the secondary device. Although the LF-FRA is not integrated into the Litz wire, LF-FRA interference can also affect wireless power transfer efficiency. An H-field check of the surfaces of the primary device and the secondary device confirms that there was no interference effect, and the results are shown in Figure 19.
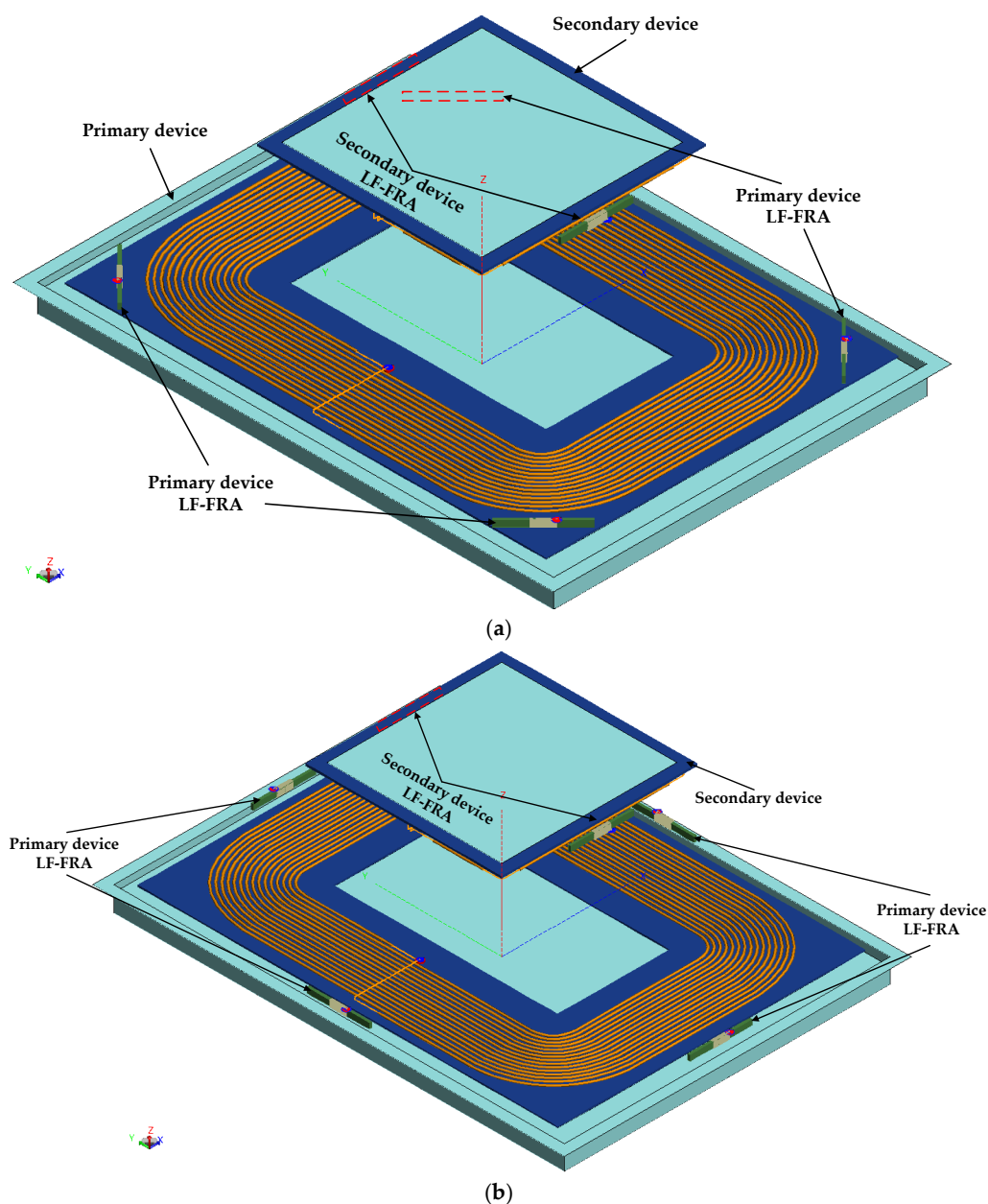
Figure 18. The geometrical structure: (**a**) the LF-FRA was arranged at each corner of the primary device, and two LF-FRAs were arranged at the center of each side of the secondary device; and (**b**) the LF-FRA was arranged at the center of each side of the primary device, and two LF-FRAs were arranged at the center of each side of the secondary device.
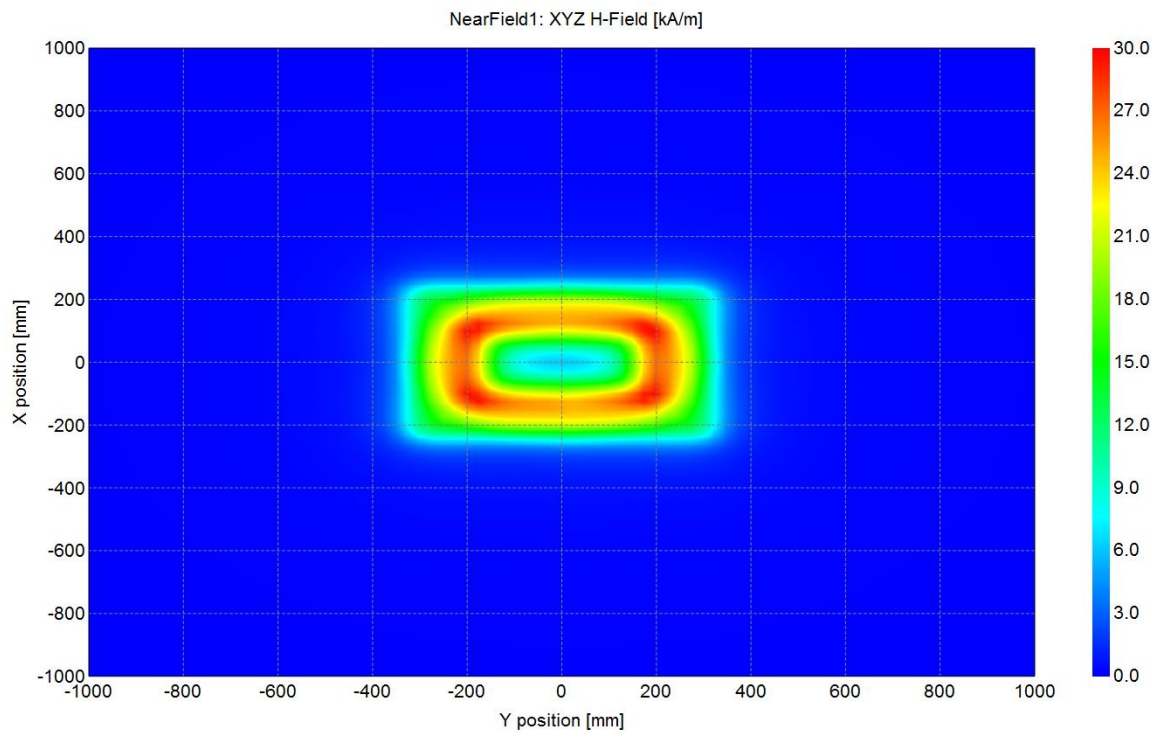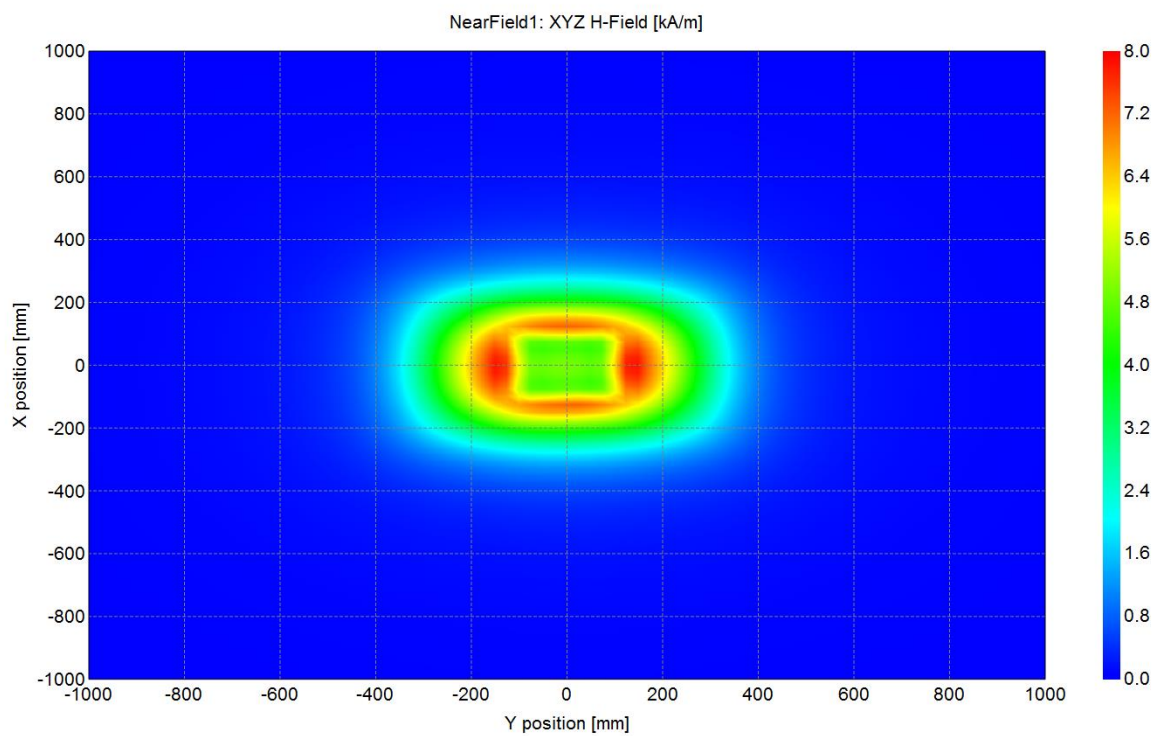
NearField1: XYZ H-Field [kA/m]

(**a**)

NearField1: XYZ H-Field [kA/m]
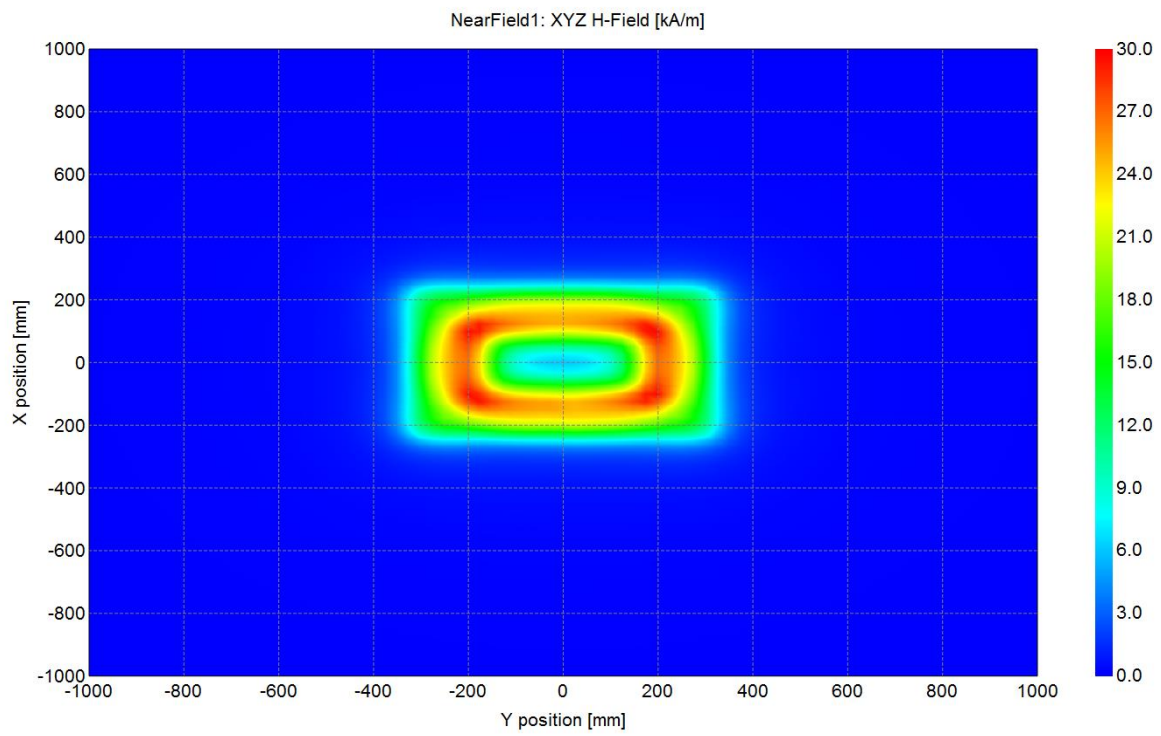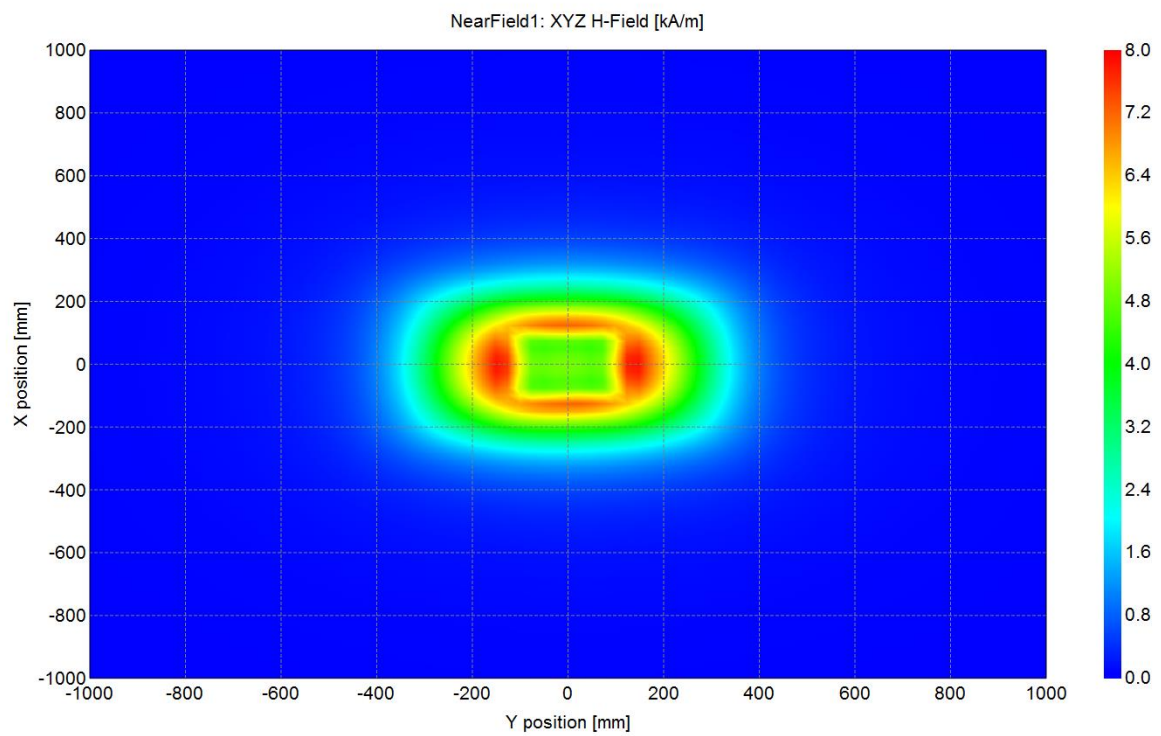
(**b**)

Figure 19. *Cont.*

(**c**)

(**d**)

Figure 19. H-field of the primary device and the secondary device according to the LF-FRA array: (**a**) the H-field in which an LF-FRA was arranged at each corner of the primary device, (**b**) the H-field in which two LF-FRAs were arranged at the center of each side of the secondary device, (**c**) the H-field in which an LF-FRA was arranged at the center of each side of the primary device, and (**d**) the H-field in which two LF-FRAs were arranged at the center of each side of the secondary device.

From the pattern of the near-field B-field, the B-field distance according to the arrangement of the LF-FRA was predicted. When an LF-FRA was arranged at each corner of the primary device, the distance of the B-field with a value of 4 nT was a total 1.79 m. Here, the distance of the B-field, with the LF-FRA of the secondary device having a value of 4 nT, was a total of 1.56 m. Similarly, when the LF-FRA was arranged at the center of each side of the primary device, and the secondary device was used with two LF-FRAs, the distance of the B-field with a value of 4 nT was a total of 1.59 m and 1.46 m, respectively. The simulation results for the B-field are shown in Figure 20. Therefore, when fine positioning was performed on the LF-FRA, the B-field transmission and reception distances were 1.675 m and 1.525 m, respectively. If only the distance was considered, the arrangement was confirmed to be best when an LF-FRA was placed at each corner of the primary device.
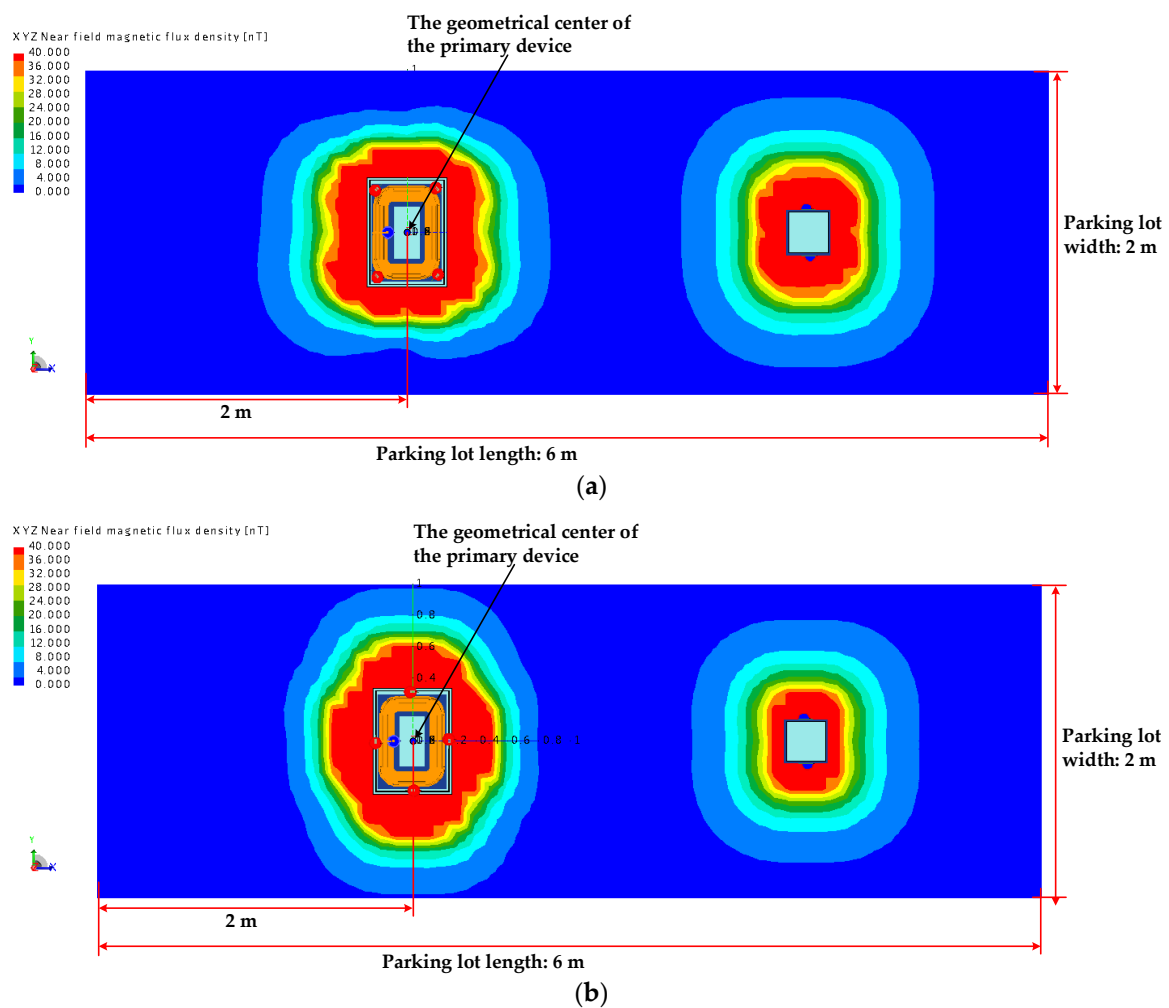

(**a**)

(**b**)

Figure 20. The pattern of the near-field B-field: (**a**) the LF-FRA was arranged at each corner of the primary device, and two LF-FRAs were arranged at the center of each side of the secondary device; and (**b**) the LF-FRA was arranged at the center of each side of the primary device, and two LF-FRAs were arranged at the center of each side of the secondary device.

5.3. LF-FRA Fine Positioning Optimization

As a fine positioning method for EV MF-WPT, LF-FRA showed an excellent performance. However, the LF-FRA that wound in one direction had some limitations due to the characteristics of the B-field. First, due to the physical characteristic of the LF-FRA, the received LF-FRA did not have a good resolution. Therefore, the difference between the B-fields accepted by the receiving LF-FRA should be at least 2 dB. Second, if the angle between the two antennas was 90 degrees, the receiving LF-FRA

did not recognize the B-field of the transmitting LF-FRA. This was because of the inherent physical properties of the magnetic field. Due to these constraints, when the primary device and the secondary device began to overlap (more precisely, when the B-field of the LF-FRA of the primary device and the B-field of the LF-FRA of the secondary device began to overlap), the LF-FRA acting as the receiver was sometimes unable to accurately recognize the distance.

Figure 21 shows the simulation results when the primary device and the secondary device began to overlap. The first verification took place when the LF-FRA was placed at each corner of the primary device. As the primary device overlapped the secondary device, the LF-FRA acting as a receiver lost the sine component for the relative angles to the LF-FRA of the primary device and to the LF-FRA of the secondary device. Therefore, it was difficult to recognize the B-fields transmitted from the four LF-FRAs of the primary device with the two LF-FRAs of the secondary device. In the opposite case, it was also difficult to recognize the B-fields transmitted from the two LF-FRAs of the secondary device with the four LF-FRAs of the primary device. The second validation took place when the LF-FRA was placed at the center of each side of the primary device. As the primary device overlapped the secondary device, the LF-FRA in the x-direction of the primary device and the LF-FRA in the −x-direction of the secondary device momentarily had a relative angle of 90 degrees. The fact that the relative angle was 90 degrees meant that since the B-field was the value of the vector, the LF-FRA acting as the receiver did not recognize the B-field. Finally, fine positioning for the EV MF-WPT also needed to consider the z-direction. If the theory of static magnetic fields [34] is used, the z-direction can be confirmed with the B-field transmitted from the small loop antenna to any point. The B-field is given by:

$$\vec{B_z} = \frac{\mu_0 m}{4\pi r^3}\left(2\cos\theta^2 - \sin\theta^2\right)\vec{z},\tag{19}$$

where *r* is the distance between the small loop antenna and any point, μ_0 is the permeability of free space, *m* is the magnetic dipole moment, and θ is the angle between the small loop antenna and any point. The results of graphing the B-field of the z-direction using the MATLAB software from MathWorks [42] are shown in Figure 22.
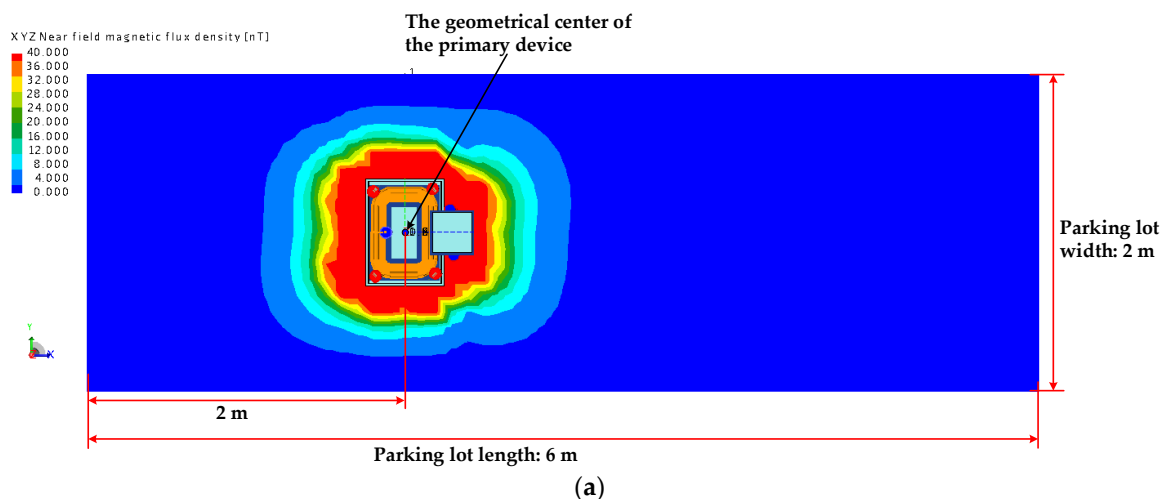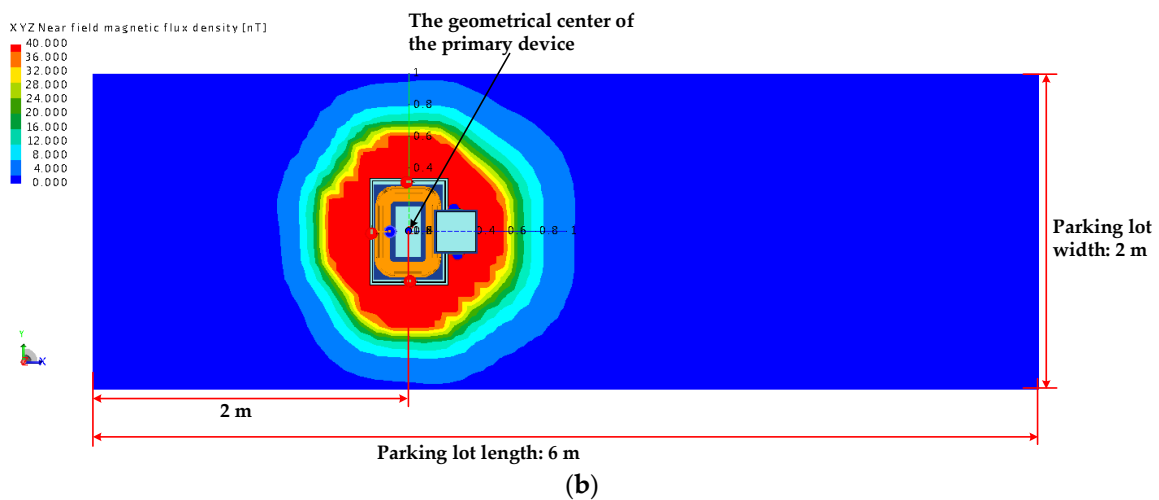

Figure 21. *Cont.*

(b)

Figure 21. The pattern of the near-field B-field when the primary device and the secondary device began to overlap: (**a**) The LF-FRA was arranged at each corner of the primary device, and two LF-FRAs were arranged at the center of each side of the secondary device; and (**b**) the LF-FRA was arranged at the center of each side of the primary device, and two LF-FRAs were arranged at the center of each side of the secondary device.
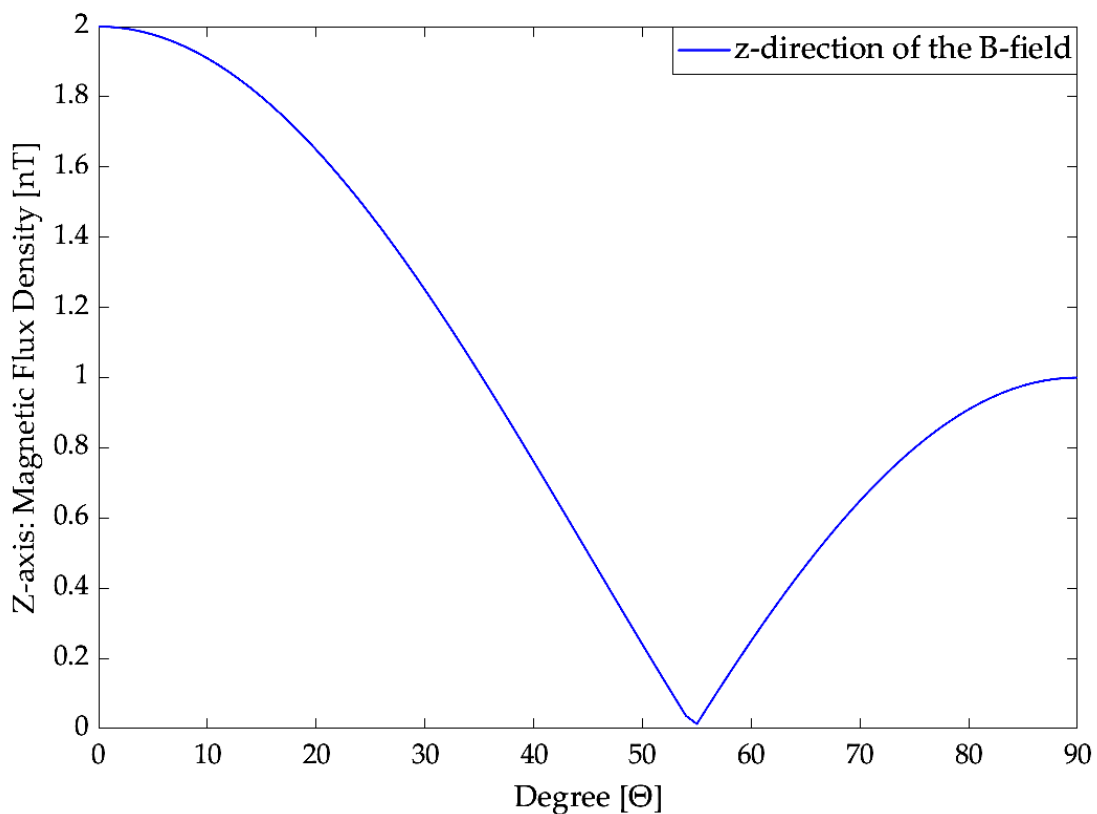

Figure 22. The z-direction of the B-field transmitted from the small loop antenna to any point.

Therefore, in order to solve this problem, it was necessary to create a case where the angle difference between the LF-FRA of the primary device and the LF-FRA of the secondary device was 0 degrees. The primary device needed to have a method of positioning the LF-FRA array at the center of each side. The secondary device needed to add another LF-FRA located at the center of each side. In order to apply to an EV, it was also necessary to consider production costs. Thus, there was a need to reduce by one the number of LF-FRAs applied to the primary device. In summary, the LF-FRA was arranged at the center of

each side of the primary device and of the secondary device. Moreover, there were three LF-FRAs each for the primary device and the secondary device. Figure 23 shows the geometrical structure in which the LF-FRAs were rearranged on the primary device and the secondary device based on this summary. Both the primary device and the secondary device had LF-FRAs arranged in the ±y-directions. The number of cases where LF-FRAs could be arranged could be divided into four, in which LF-FRAs were arranged in the ±x-direction on the primary device or on the secondary device.

(**a**)

(**b**)
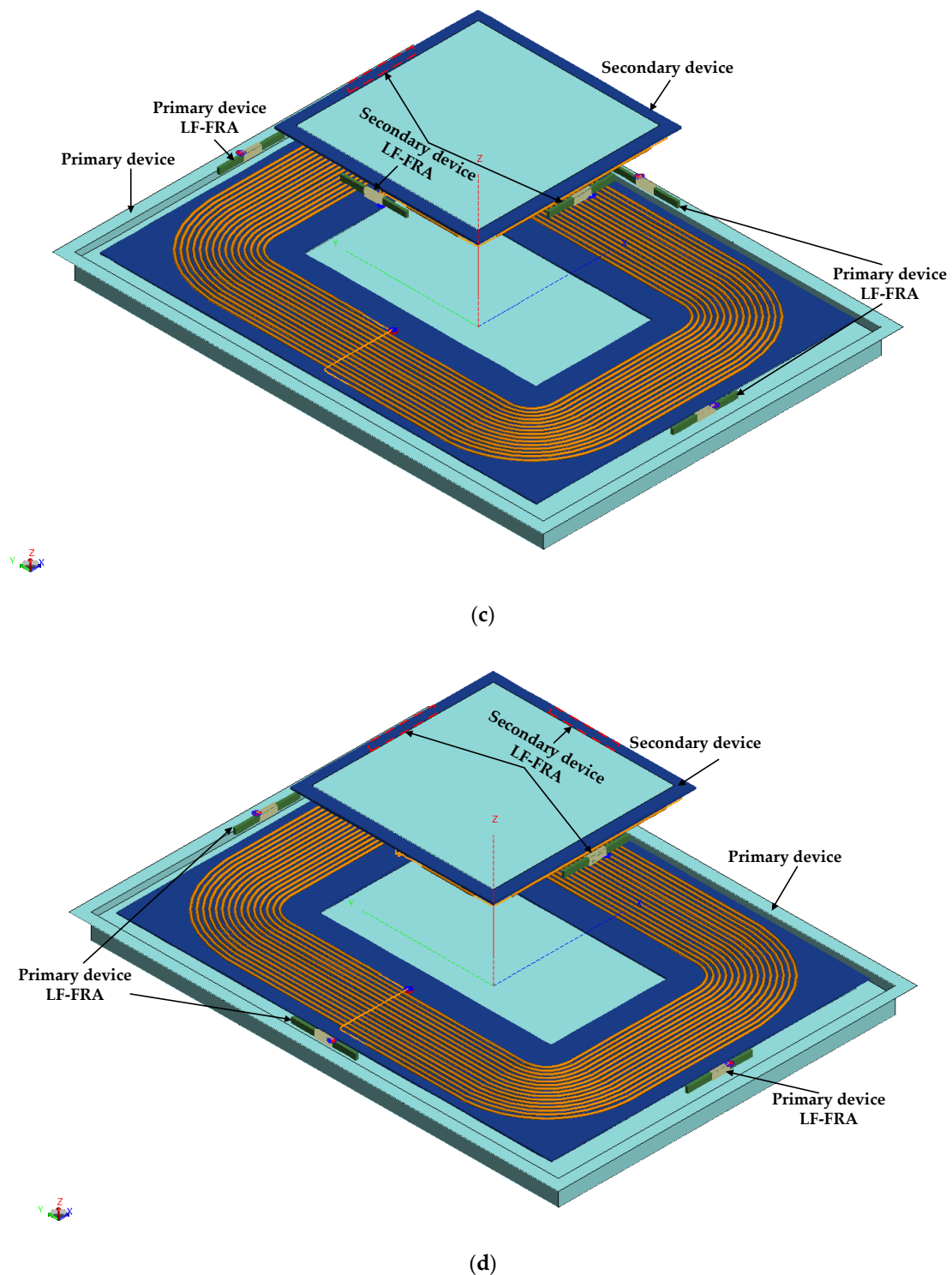
Figure 23. *Cont.*

(**c**)

(**d**)
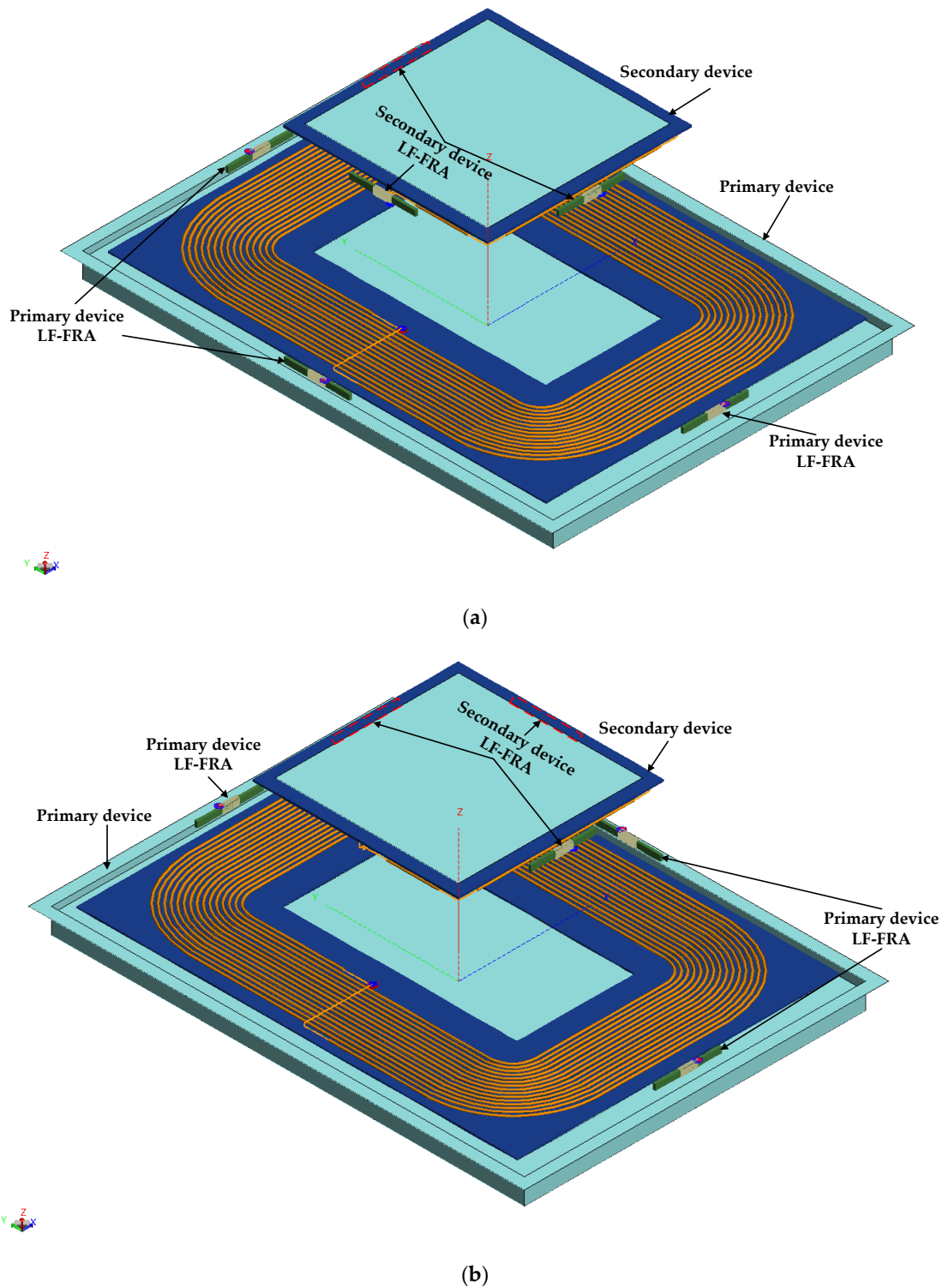
Figure 23. The geometrical structure: (**a**) the LF-FRA located on both the primary device's and the secondary device's −x-direction, (**b**) the LF-FRA located on both the primary device's and the secondary device's x-direction, (**c**) the LF-FRA located on the primary device's x-direction and the secondary device's −x-direction, and (**d**) the LF-FRA located on the primary device's −x-direction and the secondary device's x-direction.

Based on this summary, the simulation results for the B-field in which the LF-FRA was arranged on the primary device and the secondary device are shown in Figure 24. The value of the recognition distance of the B-field used for fine positioning was the sum of the distance from the geometrical

center of the primary device to the B-field formed by the x-direction and the secondary device to the B-field formed by the −x-direction, as shown in Table 4. Based on the simulation results, the optimal arrangement of the LF-FRA for fine positioning of the EV MF-WPT was to arrange the LF-FRA in the −x- and ±y-direction for the primary device and x- and ±y-direction for the secondary device.

(a)

(b)

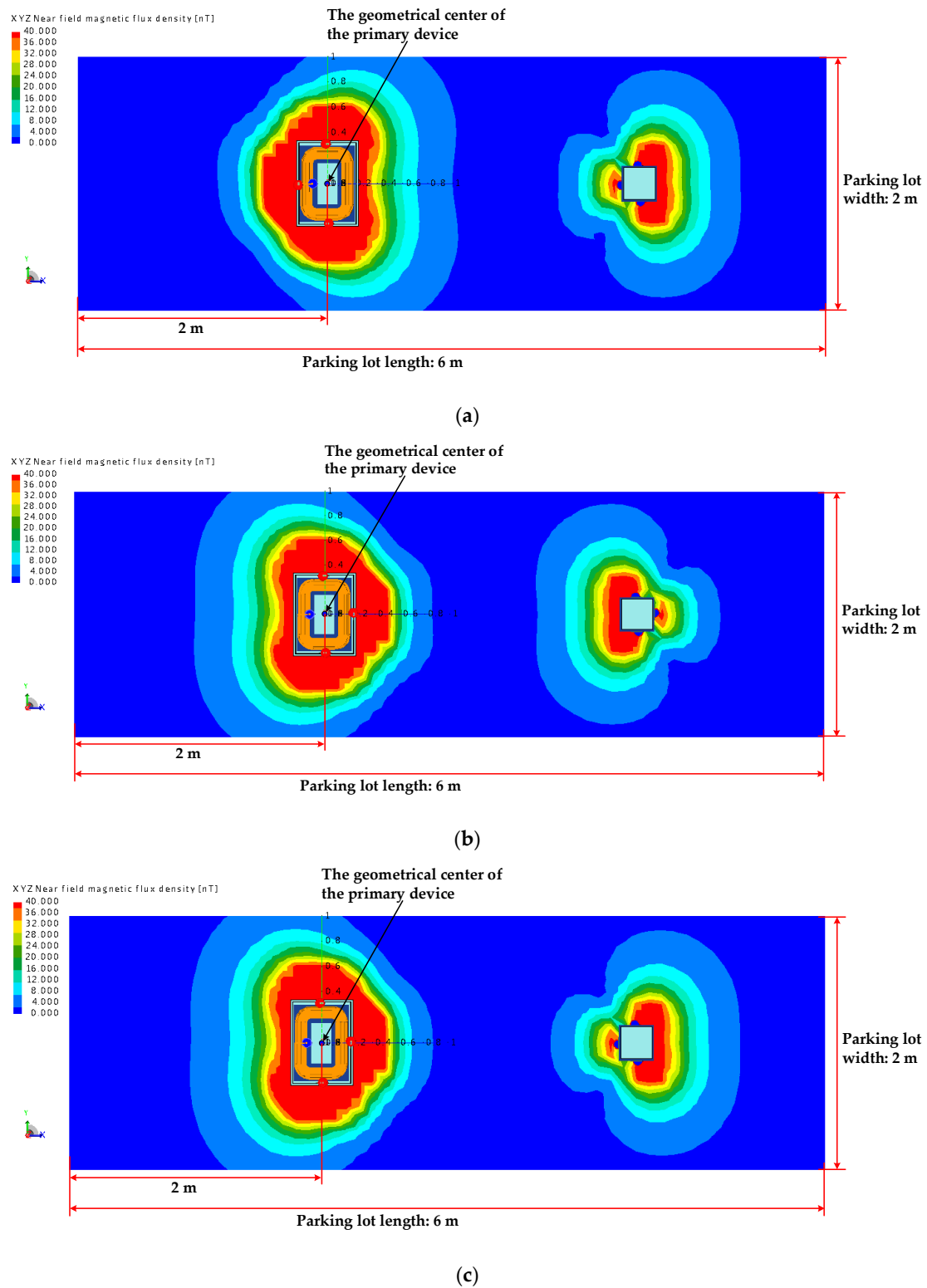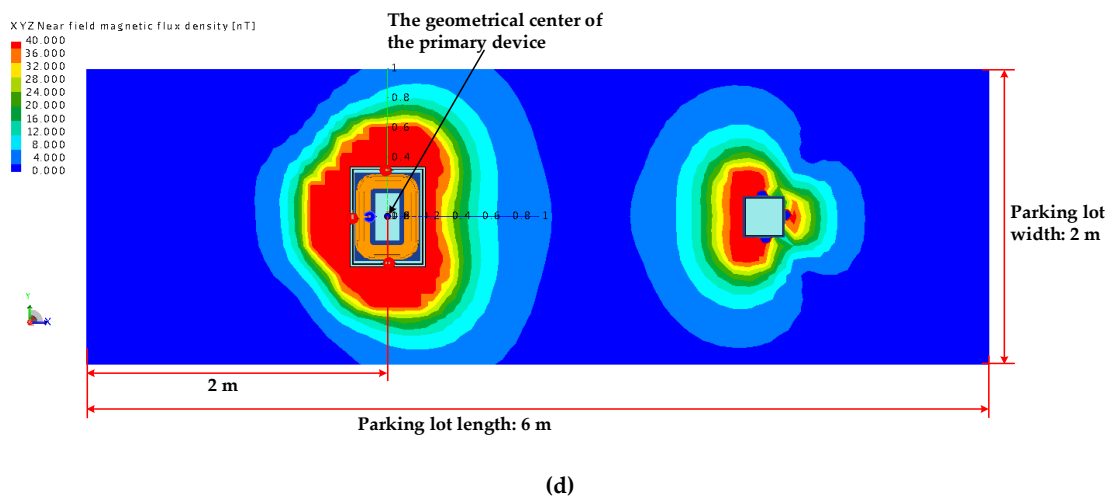
(c)

Figure 24. *Cont.*

(d)

Figure 24. The pattern of the near field B-field: (**a**) the LF-FRA located on both the primary device's and the secondary device's −x-direction, (**b**) the LF-FRA located on both the primary device's and the secondary device's x-direction, (**c**) the LF-FRA located on the primary device's x-direction and the secondary device's −x-direction, and (**d**) the LF-FRA located on the primary device's −x-direction and the secondary device's x-direction.

**Table 4.** The value of the recognition distance of the B-field used for fine positioning (m).

The Primary Device LF-FRA Position	The Secondary Device LF-FRA Position	Total B-Field Distance
−x direction: 1.01	−x direction: 0.67	1.68
+x direction: 0.87	+x direction: 0.81	1.68
+x direction: 0.88	−x direction: 0.69	1.57
−x direction: 1.09	+x direction: 0.90	1.99

Figure 25 shows the simulation results when the primary device and the secondary device begin to overlap, with the LF-FRA arranged in an optimal location for the primary device and the secondary device. For the simulation results, it is necessary to separate the roles of the transmitting LF-FRA and the receiving LF-FRA. Thus, in this paper, the LF-FRA of the primary device was the LF-FRA on the receiving side, and the LF-FRA of the secondary device was the LF-FRA on the transmitting side. There were a total of nine cases where confirmation was required, but we describe only four here. Please refer to Appendix A for the remaining details. First, the LF-FRA in the x-direction of the secondary device transmitted the magnetic field, and the LF-FRA in the −y-direction of the primary device received the magnetic field (see Figure 25a). Since the LF-FRA in the −y-direction of the primary device and the LF-FRA in the x-direction of the secondary device were orthogonal, it was possible to confirm that the B-field was hardly transmitted. Theoretically, the B-field should not be transmitted perfectly; however, since the B-field's actual shape had a spatial size, the vector direction of the magnetic field was not perfectly orthogonal, so energy could be transmitted. The energy delivered was very low compared to the energy delivered when the direction was the same. Second, the LF-FRA in the x-direction of the secondary device transmitted the magnetic field, and the LF-FRA in the y-direction of the primary device received the magnetic field (see Figure 25b). It was confirmed that the result was the same as the first case. Third, the LF-FRA in the x-direction of the secondary device transmitted the magnetic field, and the LF-FRA in the −x-direction of the primary device received the magnetic field (see Figure 25c). Since the direction of the LF-FRA was the same, it was confirmed that the energy was transmitted well. Finally, the LF-FRA transmitted the magnetic field in all directions of the secondary device, and the LF-FRA received the magnetic field in all directions of the primary device (see Figure 25d–f). In other words, the geometric center of the primary device and the geometric center of the secondary device were perfectly aligned. Since all directions of the LF-FRA were the same, it was confirmed that the energy is transmitted well. Based on the simulation

results, we confirmed that the LF-FRA arrangement we proposed was well recognized, even when the primary device and the secondary device began to overlap.
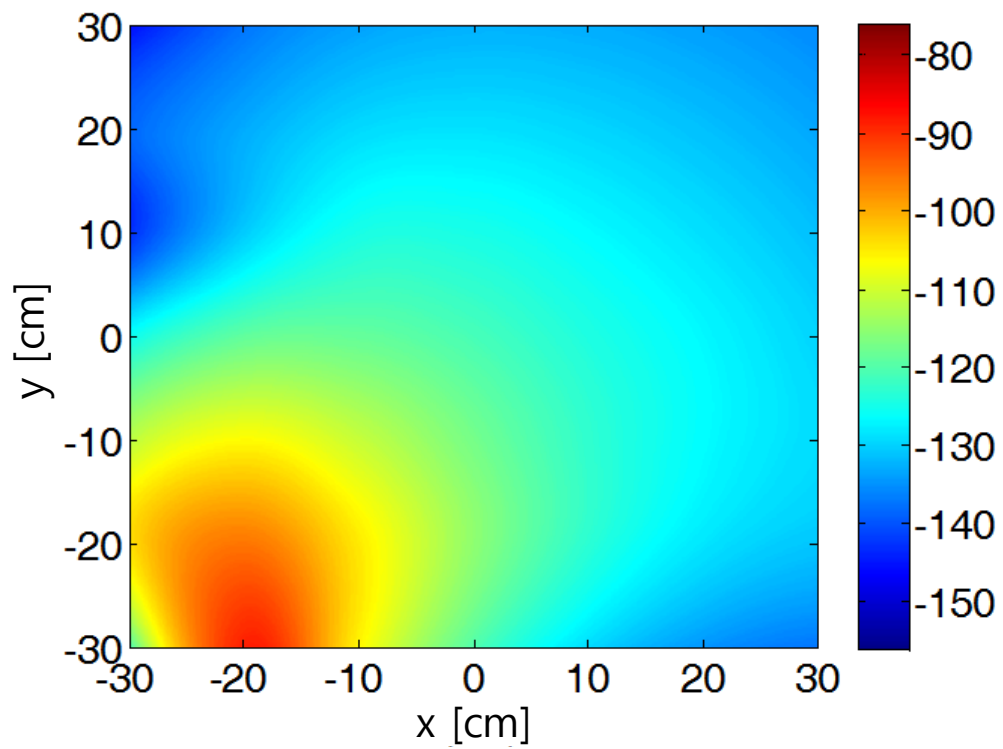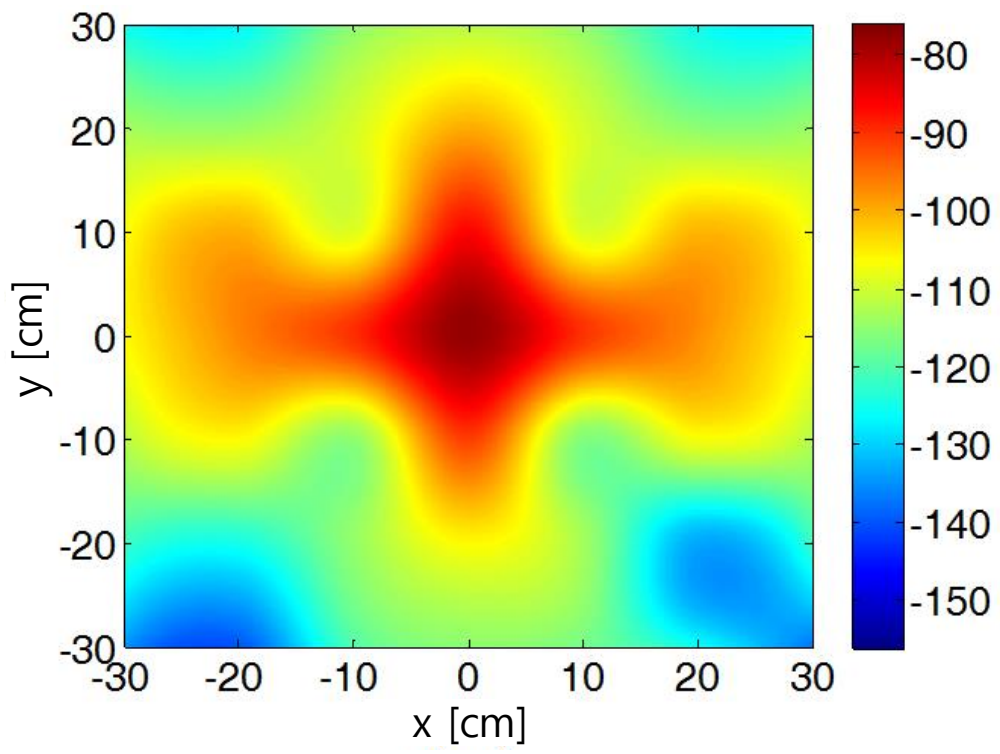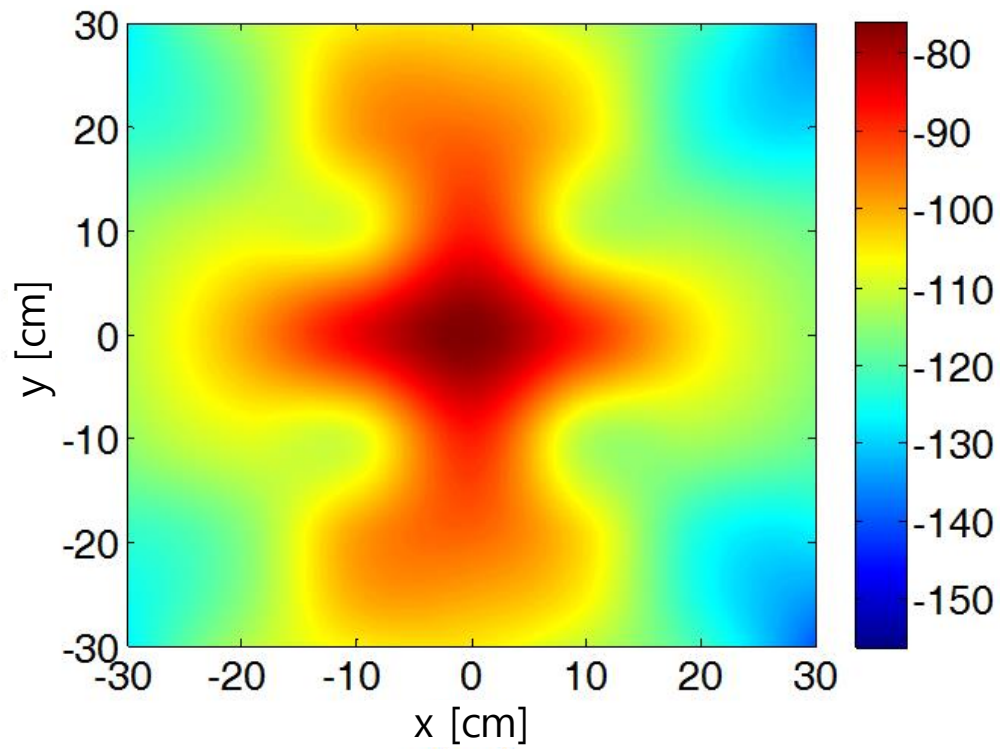

(a)
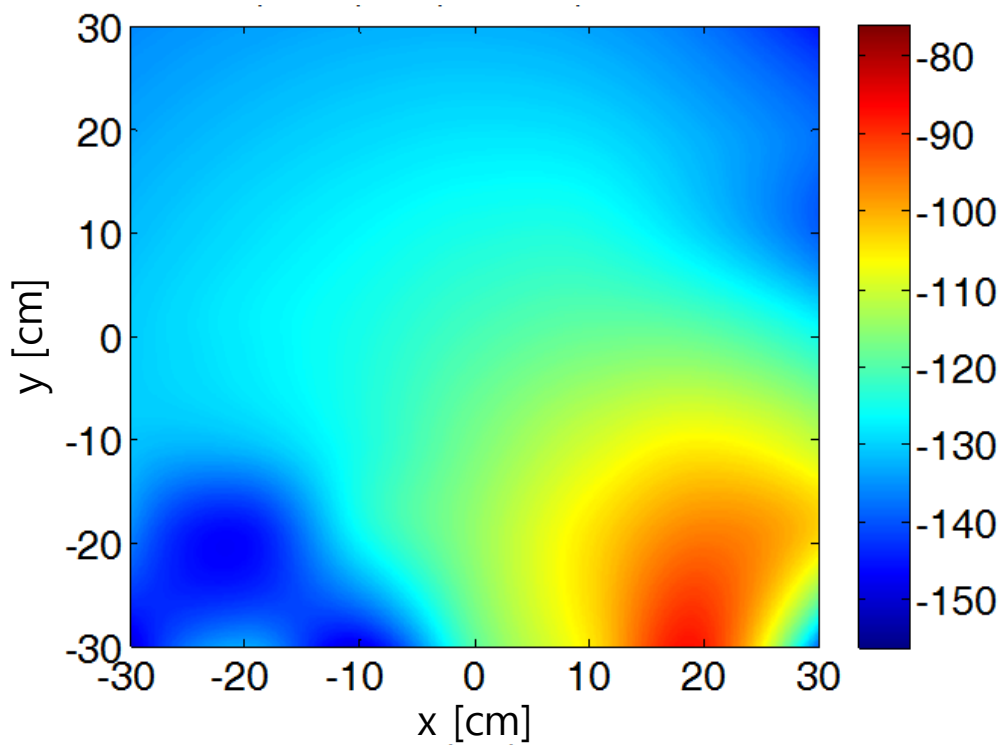
(b)

Figure 25. *Cont.*

(**c**)

(**d**)

Figure 25. *Cont.*
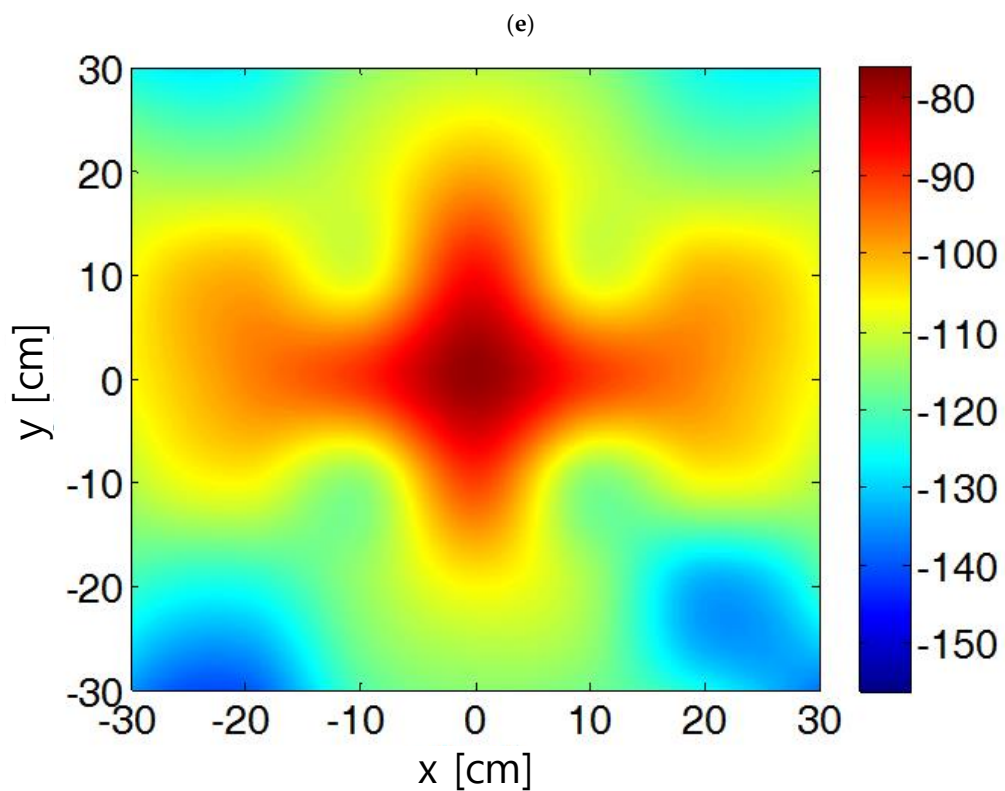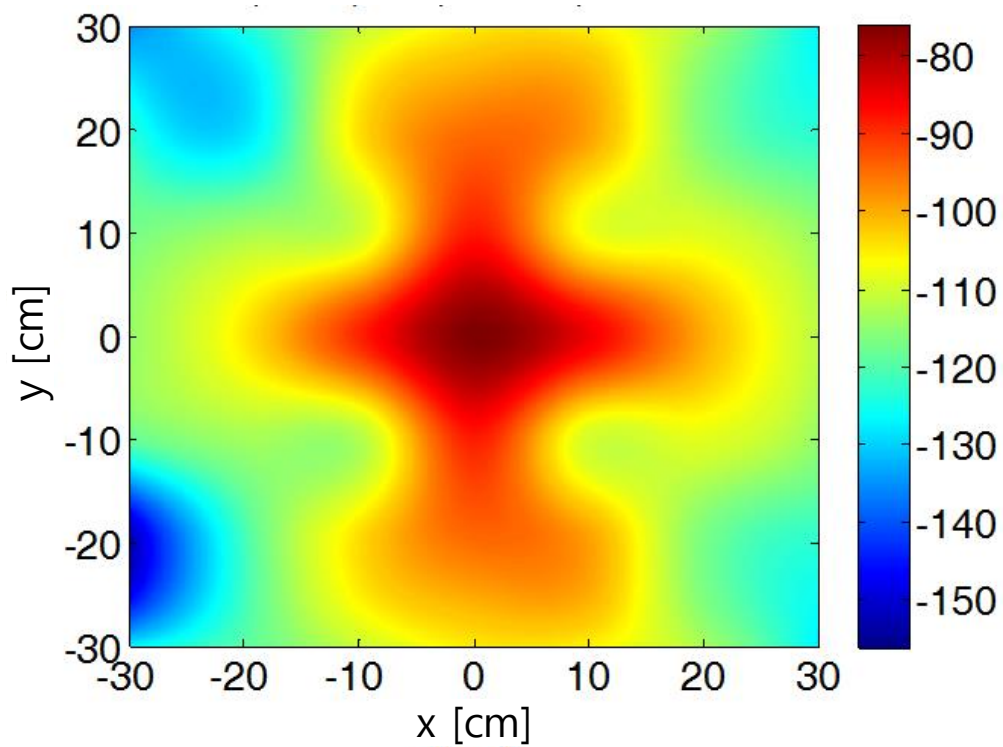
(**e**)

(**f**)

Figure 25. The near-field B-field of the LF-FRA arranged at an optimal location for the primary device and the secondary device: (**a**) the LF-FRA in the x-direction of the secondary device transmitter and the LF-FRA in the −y-direction of the primary device receiver; (**b**) the LF-FRA in the x-direction of the secondary device transmitter and the LF-FRA in the y-direction of the primary device receiver; (**c**) the LF-FRA in the x-direction of the secondary device transmitter, the magnetic field, and the LF-FRA in

the −x-direction of the primary device receiver; (**d**) when the primary device and the secondary device were perfectly aligned, the LF-FRA was in the −y-direction of the secondary device transmitter and the LF-FRA was in the −y-direction of the primary device receiver; (**e**) when the primary device and the secondary device were perfectly aligned, the LF-FRA was in the y-direction of the secondary device transmitter the magnetic field and the LF-FRA was in the y-direction of the primary device receiver; (**f**) when the primary device and the secondary device were perfectly aligned, the LF-FRA was in the x-direction of the secondary device transmitter and the LF-FRA was in the −x-direction of the primary device receiver.

6. Experiments

In order to confirm the optimal LF-FRA arrangement for fine positioning, the experimental test used an MF-WPT integrated into a KIA SOUL. Figure 26 shows the test bench for the fine positioning of the EV MF-WPT and the test case for each region for measuring. A ROHDE and SCHWARZ SMC100A signal generator [43] was used as the instrument for generating a magnetic field in the transmitting LF-FRA integrated into the secondary device; this instrument can provide power at a specific frequency. The instrument for measuring the B-field of the receiving LF-FRA integrated into the primary device was an RTE 1104 oscilloscope [44] from ROHDE and SCHWARZ, which can measure various values at a given frequency. The instrument used to enable the secondary device to move into the primary device was the WPT Testing Platform from Chroma [45], which allows a primary device to be moved on the ±x-, ±y-, and ±z-directions. The reason for moving the primary device on this test bench was to use it for actual vehicle-level evaluation. To perform a test for alignment, the secondary device needed to move in millimeters. However, it is almost impossible for a vehicle to move in millimeters with a secondary device installed on the vehicle.
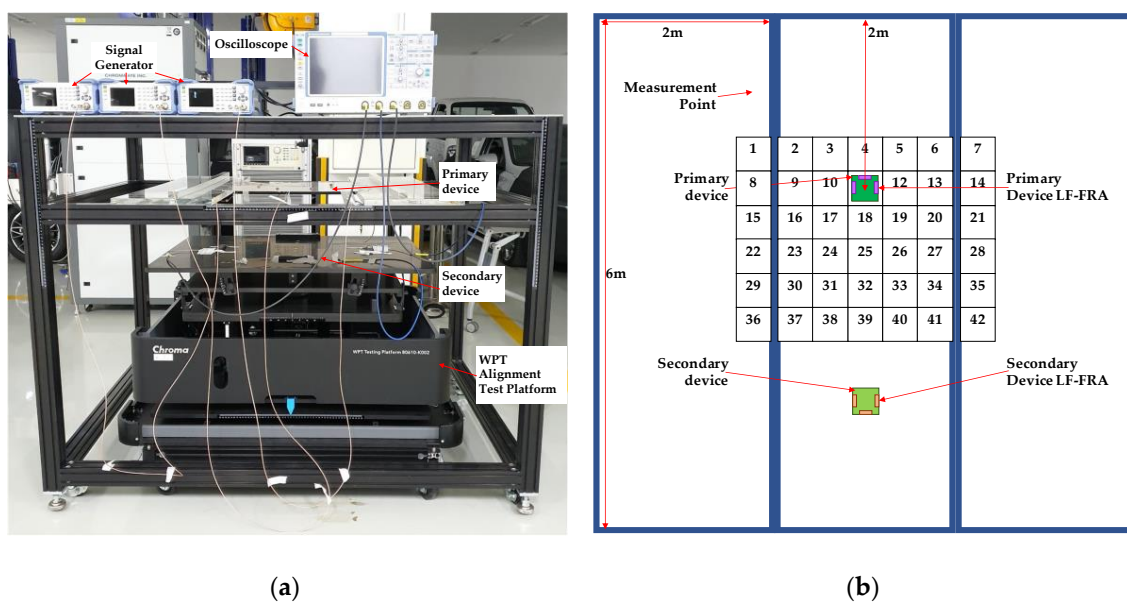

(**a**)

(**b**)

Figure 26. The experimental test condition: (**a**) the EV MF-WPT fine positioning test bench and (**b**) the EV MF-WPT fine positioning test case.

The results of the oscilloscope measurement waveform for the power of the receiving LF-FRA on the primary device are shown in Figure 27 and simply described in Table 5. Please refer to Appendix B for the results at all measurement points. Since the LF-FRA in the −x-direction of the primary device was in region 11, the output of the LF-FRA in the −x-direction of the primary device increased when the LF-FRA in the x-direction of the secondary device entered measurement points 39, 32, 25, 18, 11, and 4. In particular, measurement point 11 was confirmed to have the highest output because the primary device and the secondary device were perfectly aligned. The same was seen for the LF-FRA in the ±y-direction of

the primary device and the secondary device. If the difference between the primary device's y-direction output and −y-direction output was within 2 dB, the secondary device was located on the centerline of the primary device. The point where the primary device's LF-FRA output was the highest and the difference between the y-direction's output and the −y-direction's output of the primary device was within 2 dB was confirmed through the data for measurement point 11. This also meant that the primary device and the secondary device were perfectly aligned. The left side measurement results for measurement points 39, 32, 25, 18, 11, and 4 indicated that the −y-direction's output of the primary device was higher than the y-direction's output. This meant that the secondary device needed to be moved to the right. The right-side measurement results of measurement points 39, 32, 25, 18, 11, and 4 were also similar to those of the left-side measurements. In other words, the y-direction output of the primary device was higher than that of the −y-direction output. This meant that the secondary device needed to be moved to the left. Therefore, it can be seen that our proposal for the arrangement of LF-FRAs for the fine positioning of EV MF-WPT had the same result as the simulation and measurement results.
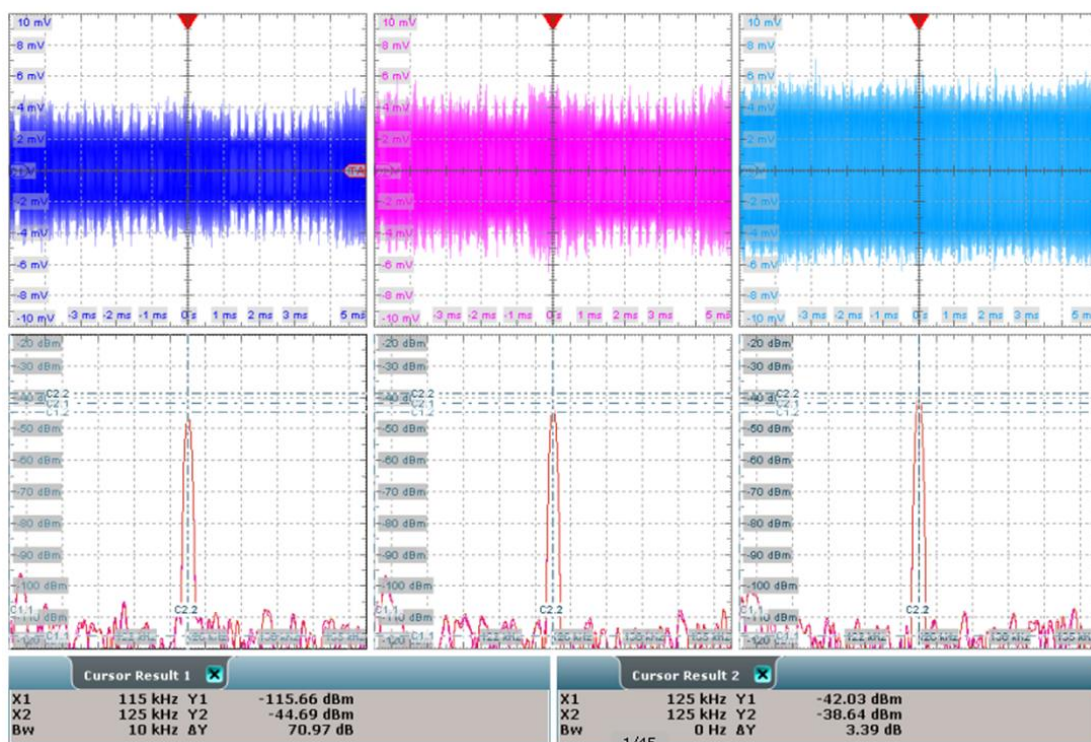

Figure 27. The oscilloscope measurement waveform for the power of the receiving LF-FRA on the primary device.

Table 5. The measurement results of the receiving LF-FRA power integrated into the primary device (dBm).

Test Region [1]	Primary Device		
	−x-Direction	−y-Direction	y-Direction
3	−40.97	−26.74	−50.93
4	−34.18	−29.86	−30.07
5	−41.23	−51.25	−24.89
10	−27.55	−9.93	−42.37
11	−9.29	−18.51	−19.85
12	−28.10	−40.00	−10.65
17	−43.67	−26.22	−51.44
18	−38.45	−30.00	−29.15
19	−43.37	−51.06	−23.90

[1] Refer to Appendix B for results at all measurement points.

7. Conclusions

In this study, we designed and modeled an optimized arrangement of a LF-FRA for the fine positioning of an EV MF-WPT in accordance with IEC 61980 and SAE J2954 standards. First, based on the theoretical background of antenna theory, the basic design and model of the LF-FRA that were most suitable for fine positioning were reviewed in advance. In addition, positioning techniques were investigated in advance, and the method of positioning in three dimensions was reviewed. Second, we pre-qualified the EV MF-WPT system and LF-FRA using simulation software widely used in industry and academia. For EV MF-WPT systems, electrical circuits with output power levels up to 7.7 kVA for supplies and input power levels up to 3.7 kVA for EV devices were built using Maxwell 3D and Simplorer. The geometric dimensions of the LF-FRA for fine positioning of an EV MF-WPT confirmed the pre-condition that it might have 70 turns on a ferrite rod width of 90 mm, length of 10 mm, and thickness of 2.5 mm. Third, since the LF-FRA had to be mounted and arranged on the primary and secondary devices, the size needed to be optimized. Through modeling and simulation, we optimized the LF-FRA for EV MF-WPT fine positioning. The B-field of the LF-FRA, which was reviewed in advance, should not change and should be small enough to be mounted on the primary device and the secondary device; therefore, we finally confirmed that the optimal LF-FRA for the fine positioning of an EV MF-WPT needed to have a width of 50 mm, a length of 10 mm, a thickness of 2.5 mm, and 200 turns. Finally, two conditions were considered regarding the arrangement of LF-FRAs in the primary device and the secondary device. The first condition was the near field B-field distance of the LF-FRA. In other words, the near field B-field distance used for fine positioning was the distance from the geometrical center of the primary device to the B-field formed by the x-direction and the secondary device in the B-field formed by the −x-direction. The second condition was as follows: Even if the B-field of the LF-FRA of the primary device overlapped with the B-field of the secondary device, the LF-FRA, acting as a receiver, should have been able to accurately recognize the distance. Therefore, the optimal arrangement of the LF-FRA for the fine positioning of an EV MF-WPT that satisfied these two conditions was to arrange the LF-FRA in the −x- and ±y-direction for the primary device and the x- and ±y-direction for the secondary device. Based on the review of the theoretical background and the pre-conditions, and the results of the modeling and simulations, the test bench was built and tested to verify our proposal. The experimental results of the LF-FRA and LF-FRA arrays optimized for the fine positioning of an EV MF-WPT were in good agreement with the simulation results.

Appendix A

Appendix A Figure A1 shows the simulation results when the primary device and the secondary device began to overlap, with the LF-FRA arranged in an optimal location for the primary device and the secondary device. There were a total of nine cases. For the first case, when the secondary device was located in the bottom-left corner of the primary device, the LF-FRA was in the x-direction of the secondary device transmitter, and the LF-FRA was in the −y-direction of the primary device receiver (see Figure A1a,b). For the second case, when the secondary device was located in the bottom-right corner of the primary device, the LF-FRA was located in the x-direction of the secondary device transmitter and the LF-FRA was located in the y-direction of the primary device receiver (see Figure A1c,d). For the third case, when the secondary device was located in the top-right corner of the primary device, the LF-FRA was in the y-direction of the secondary device transmitter, and the LF-FRA was in the −x-direction of the primary device receiver (see Figure A1e,f). For the fourth case, when the secondary device was located in the top-left corner of the primary device, the LF-FRA was in

the −y-direction of the secondary device transmitter and the LF-FRA was in the −x-direction of the primary device receiver (see Figure A1g,h). For the fifth case, when the secondary device was located on the right side of the primary device, the LF-FRA was in the −y-direction of the secondary device transmitter, and the LF-FRA was in the y-direction of the primary device receiver (see Figure A1i,j). For the sixth case, when the secondary device was located on the left side of the primary device, the LF-FRA was in the y-direction of the secondary device transmitter, and the LF-FRA was in the −y-direction of the primary device receiver (see Figure A1k,l). For the seventh case, when the secondary device was located at the bottom of the primary device, the LF-FRA was in the x-direction of the secondary device transmitter, and the LF-FRA was in the −x-direction of the primary device receiver (see Figure A1m,n). For the eighth case, when the secondary device was located at the top of the primary device, the LF-FRA was in the x-direction of the secondary device transmitter, and the LF-FRA was in the −x-direction of the primary device receiver (Figure A1o,p). For the ninth case, when the geometric center of the secondary device matched the geometric center of the primary device, the LF-FRA was in the x-direction of the secondary device transmitter, the LF-FRA was in the −x-direction of the primary device receiver, the LF-FRA was in the −y-direction of the secondary device transmitter, the LF-FRA was in the -y-direction of the primary device receiver, the LF-FRA was in the y-direction of the secondary device transmitter, and the LF-FRA was in the y-direction of the primary device receiver (see Figure A1q–t).

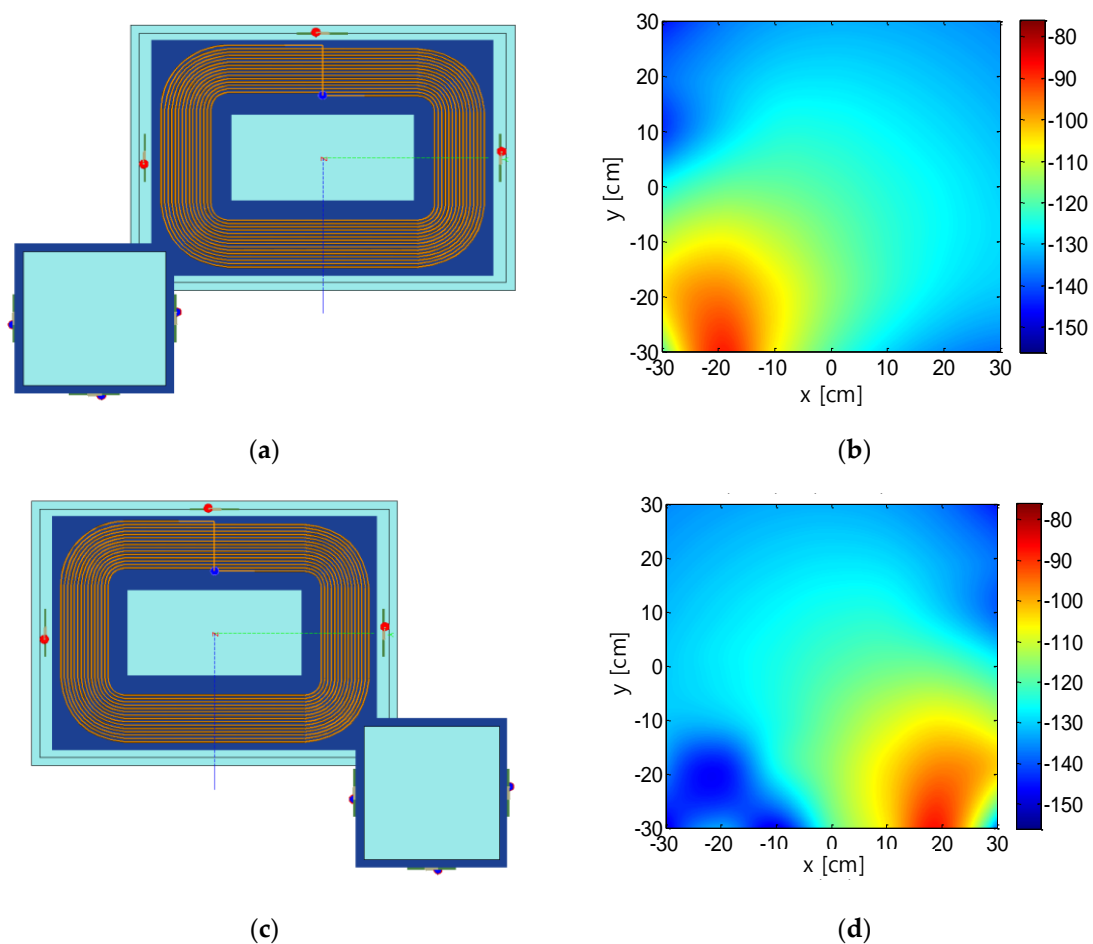
(**a**)

(**b**)

(**c**)

(**d**)

Figure A1. *Cont.*

(e)

(f)

(g)

(h)

(i)

(j)

Figure A1. *Cont.*
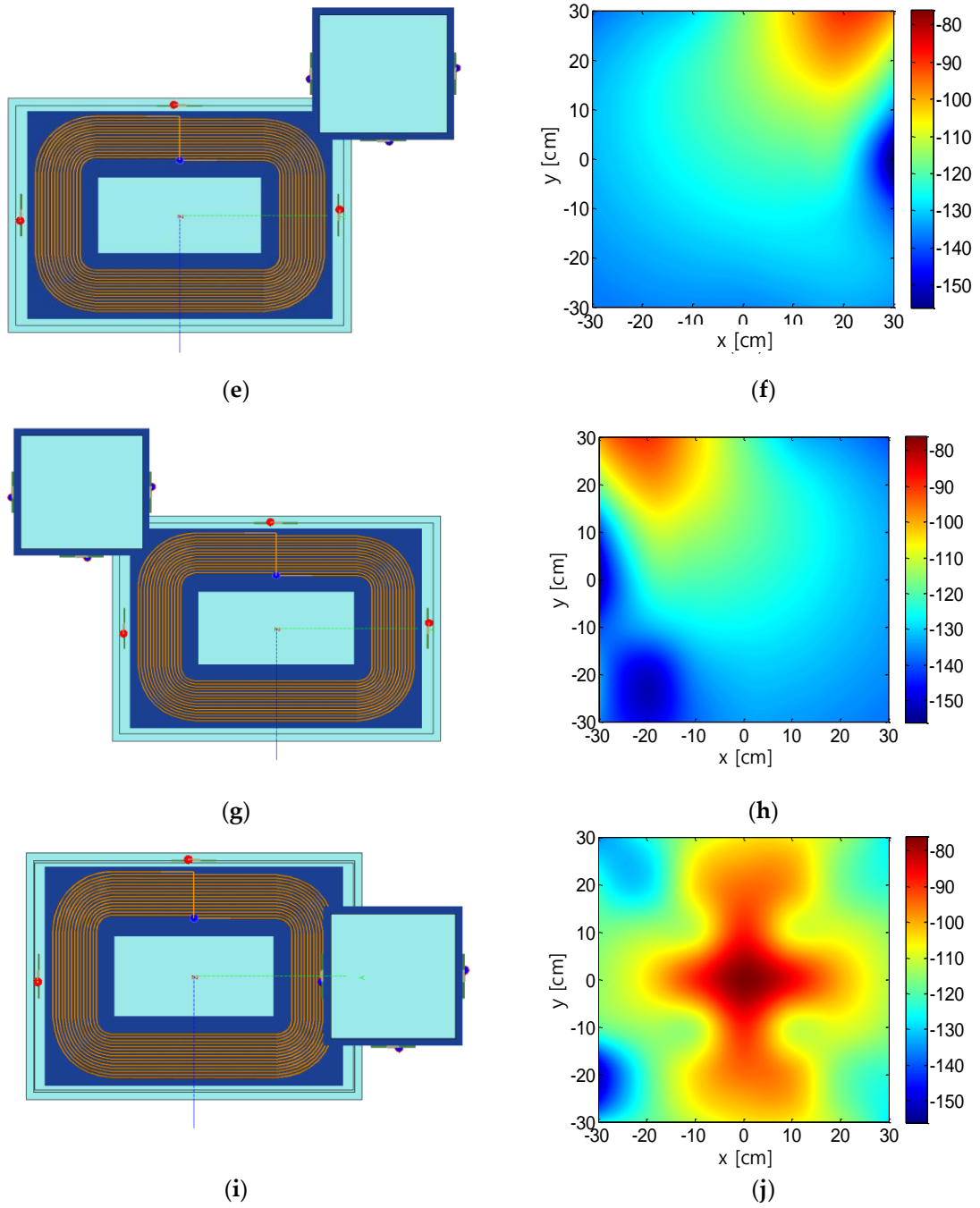
(**k**)

(**l**)
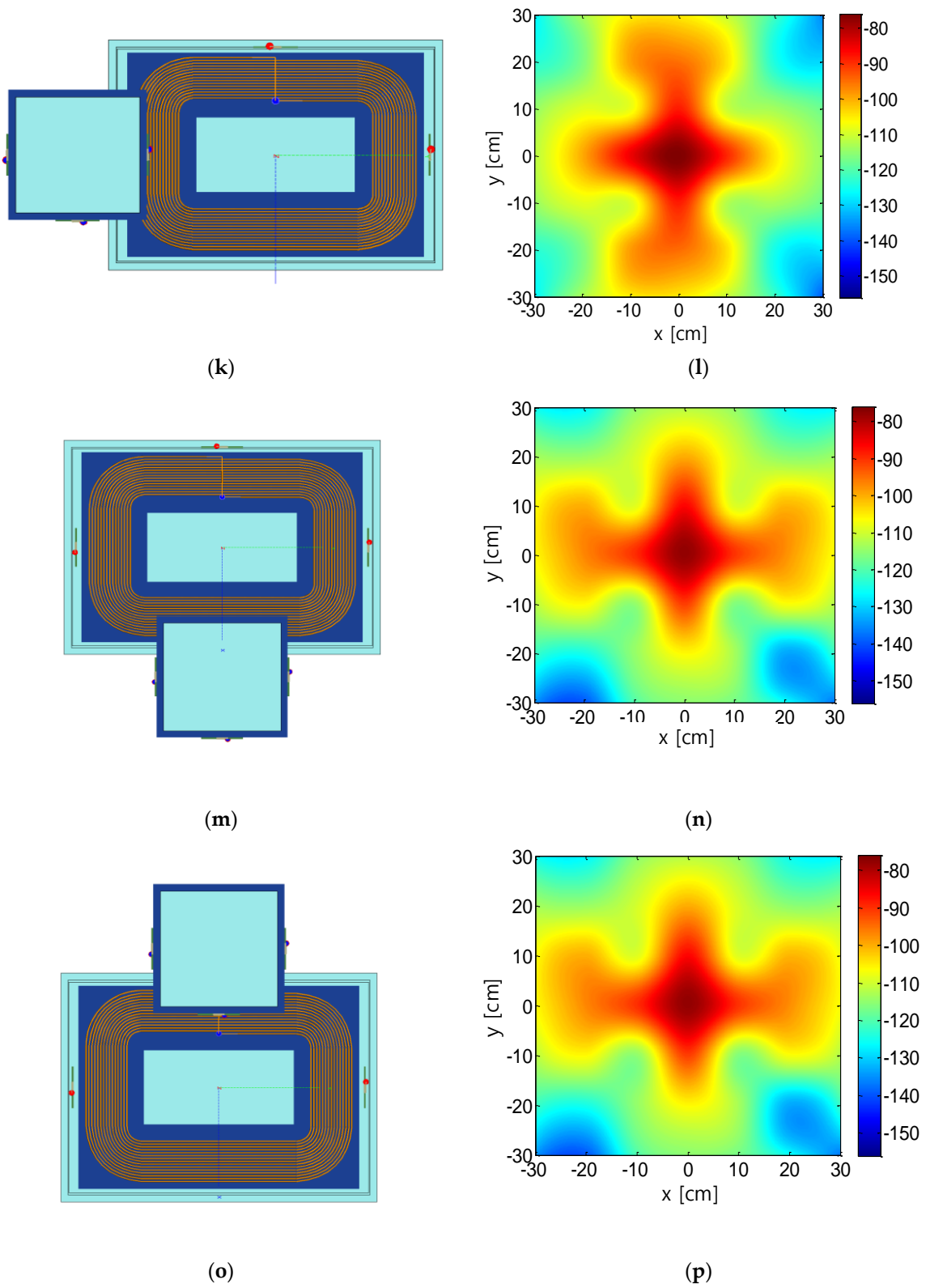

(**m**)

(**n**)

(**o**)
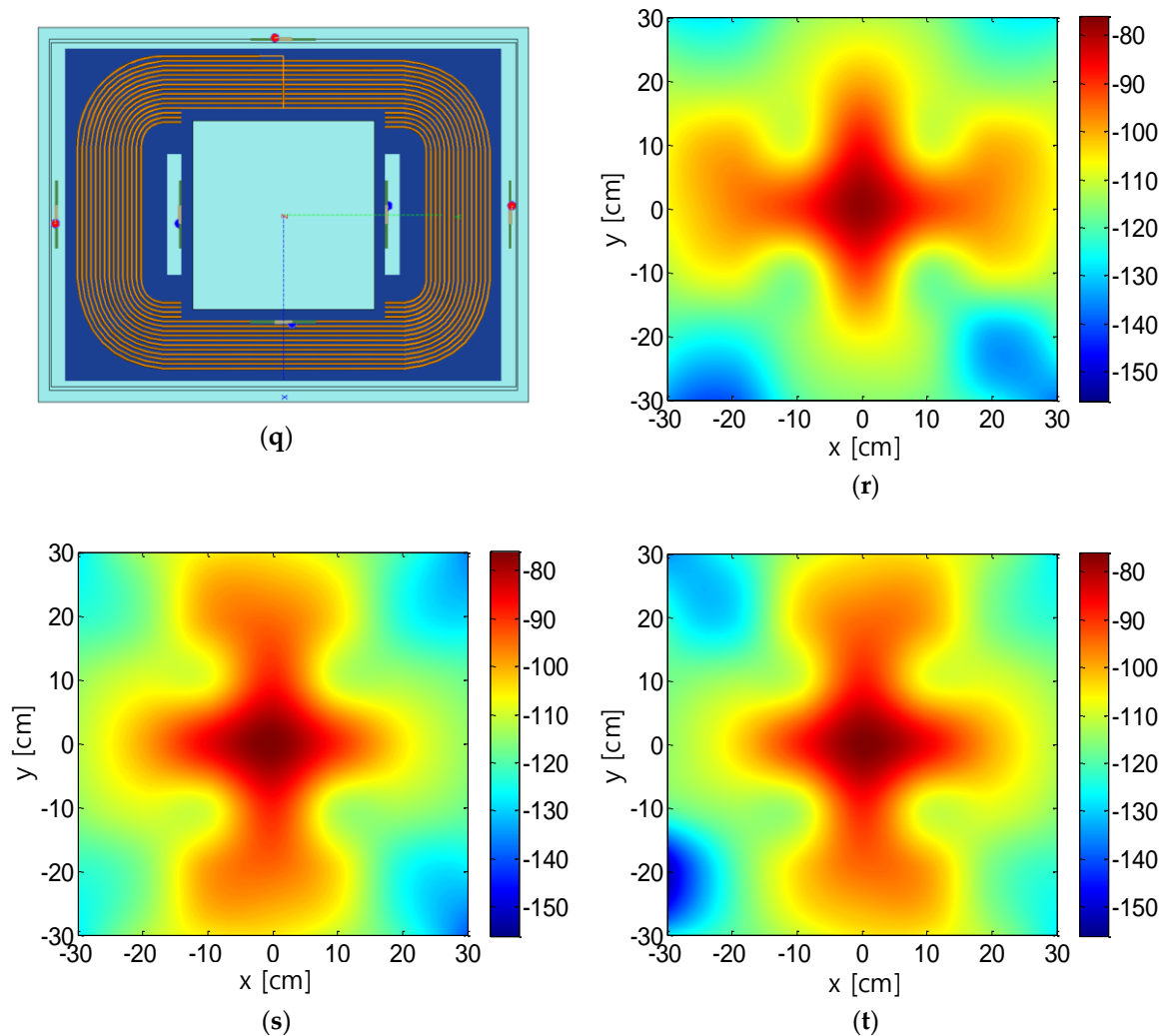

(**p**)

Figure A1. *Cont.*

Figure A1. The geometrical structure and near-field B-field of the LF-FRA arranged in an optimal location for the primary device and the secondary device: (**a**) the secondary device was located in the bottom-left corner of the primary device; (**b**) the LF-FRA in the x-direction of the secondary device transmitter and the LF-FRA in the −y-direction of the primary device receiver; (**c**) the secondary device was located in the bottom-right corner of the primary device; (**d**) the LF-FRA in the x-direction of the secondary device transmitter and the LF-FRA in the y-direction of the primary device receiver; (**e**) the secondary device was located in the top-right corner of the primary device; (**f**) the LF-FRA in the y-direction of the secondary device transmitter and the LF-FRA in the −x-direction of the primary device receiver; (**g**) the secondary device was located in the top-left corner of the primary device; (**h**) the LF-FRA in the −y-direction of the secondary device transmitter and the LF-FRA in the −x-direction of the primary device receiver; (**i**) the secondary device was located on the right side of the primary device; (**j**) the LF-FRA in the −y-direction of the secondary device transmitter and the LF-FRA in the y-direction of the primary device receiver; (**k**) the secondary device was located on the left side of the primary device; (**l**) the LF-FRA in the y-direction of the secondary device transmitter and the LF-FRA in the −y-direction of the primary device receiver; (**m**) the secondary device was located at the bottom of the primary device; (**n**) the LF-FRA in the x-direction of the secondary device transmitter and the LF-FRA in the −x-direction of the primary device receiver; (**o**) the secondary device was located in the top of the primary device; (**p**) the LF-FRA in the x-direction of the secondary device transmitter and the LF-FRA in the −x-direction of the primary device receiver; (**q**) the geometric center of the secondary

device matched the geometric center of the primary device; (**r**) the LF-FRA in the x-direction of the secondary device transmitter and the LF-FRA in the −x-direction of the primary device receiver; (**s**) the LF-FRA in the −y-direction of the secondary device transmitter and the LF-FRA in the −y-direction of the primary device receiver; (**t**) the LF-FRA in the y-direction of the secondary device transmitter and the LF-FRA in the y-direction of the primary device receiver.

Appendix B

Appendix B shows the results of the oscilloscope measurement waveform for the power of the receiving LF-FRA on the primary device. In other words, when the primary device and the secondary device began to overlap, the output value of the B-field received by the LF-FRA integrated into the primary device was measured. This data shows the measurement results not fully mentioned in Section 6. The red area shows that the secondary device was located at the geometric centerline of the primary device. From this result, the point with the highest output value indicated that the geometric center of the primary device perfectly matched with the geometric center of the secondary device (see Figure A2a). The blue area shows that the −y-direction output of the primary device LF-FRA was higher than the y-direction. This result meant that secondary devices need to move to the right. The green area means the opposite of the blue area (Figure A2b).

Region: 1	Region: 2	Region: 3	Region: 4	Region: 5	Region: 6	Region: 7
-56.11	-50.05	-40.97	-34.18	-41.23	-49.37	-55.69
Region: 8	Region: 9	Region: 10	Region: 11	Region: 12	Region: 13	Region: 14
-56.07	-46.76	-27.55	-9.29	-28.10	-47.24	-55.60
Region: 15	Region: 16	Region: 17	Region: 18	Region: 19	Region: 20	Region: 21
-56.25	-49.60	-43.67	-38.45	-43.37	-50.52	-55.73
Region: 22	Region: 23	Region: 24	Region: 25	Region: 26	Region: 27	Region: 28
-57.70	-55.55	-52.97	-50.62	-53.64	-55.77	-58.17
Region: 29	Region: 30	Region: 31	Region: 32	Region: 33	Region: 34	Region: 35
-60.08	-57.60	-56.40	-56.30	-56.20	-58.44	-59.70
Region: 36	Region: 37	Region: 38	Region: 39	Region: 40	Region: 41	Region: 42
-66.64	-64.23	-63.25	-61.19	-62.63	-62.59	-65.23

(**a**)

Figure A2. *Cont.*

Region: 1	Region: 2	Region: 3	Region: 4	Region: 5	Region: 6	Region: 7
-55.03 // -61.31	-51.19 // -58.97	-26.74 // -50.93	-29.86 // -30.07	-51.25 // -24.89	-55.39 // -45.99	-60.32 // -55.01
Region: 8	Region: 9	Region: 10	Region: 11	Region: 12	Region: 13	Region: 14
-48.80 // -53.50	-36.91 // -49.93	-9.93 // -42.37	-18.51 // -19.85	-40.00 // -10.65	-50.55 // -36.43	-54.80 // -47.97
Region: 15	Region: 16	Region: 17	Region: 18	Region: 19	Region: 20	Region: 21
-54.95 // -62.91	-50.92 // -59.09	-26.22 // -51.44	-30.00 // -29.15	-51.05 // -23.90	-57.61 // -46.17	-61.23 // -54.25
Region: 22	Region: 23	Region: 24	Region: 25	Region: 26	Region: 27	Region: 28
-56.63 // -63.52	-50.93 // -58.81	-44.49 // -50.57	-44.04 // -43.47	-52.99 // -43.11	-61.89 // -47.63	-66.87 // -56.53
Region: 29	Region: 30	Region: 31	Region: 32	Region: 33	Region: 34	Region: 35
-58.99 // -65.17	-56.64 // -59.68	-54.77 // -55.66	-53.28 // -52.48	-57.75 // -52.34	-61.07 // -53.20	-64.20 // -58.02
Region: 36	Region: 37	Region: 38	Region: 39	Region: 40	Region: 41	Region: 42
-63.10 // -69.78	-61.50 // -62.59	-58.98 // -60.25	-59.57 // -58.16	-61.36 // -58.53	-65.91 // -58.75	-66.38 // -61.34

(**b**)

Figure A2. The measurement results of the receiving LF-FRA power integrated into the primary device: (**a**) the output value of the B-field received by the −x-direction LF-FRA integrated into the primary device and (**b**) the output value of the B-field received by the y-direction and −y-direction LF-FRA integrated into the primary device.

References

1. Childress, D.H. *The Tesla Papers*; Adventures Unlimited Press: Kempton, IL, USA, 2000.
2. Kurs, A.; Karalis, A.; Moffatt, R.; Joannopoulos, J.D.; Fisher, P.; Soljačić, M. Wireless power transfer via strongly coupled magnetic resonances. *Science* **2007**, *317*, 83–86. [CrossRef] [PubMed]
3. Jang, Y.; Jovanovic, M.M. A contactless electrical energy transmission system for portable-telephone battery chargers. *IEEE Trans. Ind. Electron.* **2003**, *50*, 520–527. [CrossRef]
4. International Organization for Standardization Home Page. Available online: https://www.iso.org/standard/73547.html (accessed on 5 September 2019).
5. International Electrotechnical Commission Home Page. Available online: https://www.iec.ch/dyn/www/f?p=103:14:5664951394009::::FSP_ORG_ID,FSP_LANG_ID:8538,25 (accessed on 5 September 2019).
6. International Organization for Standardization Home Page. Available online: https://www.iso.org/committee/5383568.html (accessed on 5 September 2019).
7. International Electrotechnical Commission Home Page. Available online: https://www.iec.ch/dyn/www/f?p=103:14:5664951394009::::FSP_ORG_ID,FSP_LANG_ID:7948,25 (accessed on 5 September 2019).
8. Society of Automotive Engineers Home Page. Available online: https://www.sae.org/servlets/works/committeeHome.do?comtID=TEVHYB10 (accessed on 5 September 2019).
9. Society of Automotive Engineers Home Page. Available online: https://www.sae.org/servlets/works/committeeHome.do?comtID=TEVHYB6 (accessed on 5 September 2019).
10. International Electrotechnical Commission. *Electric Vehicle Wireless Power Transfer (WPT) Systems—Part 1: General Requirements*; IEC/CD 61980-1 ED2:2019; International Electrotechnical Commission: Geneva, Switzerland, 2019.

11. International Electrotechnical Commission. *Electric Vehicle Wireless Power Transfer (WPT) Systems—Part 2: Specific Requirements for Communication between Electric Road Vehicle (EV) and Infrastructure*; IEC TS 61980-2:2019; International Electrotechnical Commission: Geneva, Switzerland, 2019.

12. International Electrotechnical Commission. *Electric Vehicle Wireless Power Transfer (WPT) Systems—Part 3: Specific Requirements for the Magnetic Field Wireless Power Transfer Systems*; IEC TS 61980-3:2019; International Electrotechnical Commission: Geneva, Switzerland, 2019.

13. Society of Automotive Engineers International. *Wireless Power Transfer for Light-Duty Plug-In/ Electric Vehicles and Alignment Methodology*; SAE Recommended Practice J2954 (rev. 201904); Society of Automotive Engineers International: Troy, MI, USA, 2019.

14. International Organization for Standardization. *Electrically Propelled Road Vehicles—Magnetic Field Wireless Power Transfer—Safety and Interoperability Requirements*; ISO/DIS 19363:2019; International Organization for Standardization: Geneva, Switzerland, 2019.

15. International Organization for Standardization. *Road Vehicles–Three-Dimensional Reference System and Fiducial Mark–Definitions*; ISO 4130:1978; International Organization for Standardization: Geneva, Switzerland, 1978.

16. ITU. *Radio Regulations (Edition 2016)*; International Telecommunication Union: Geneva, Switzerland, 2016.

17. International Organization for Standardization. *Road Vehicles–Vehicle to Grid Communication Interface–Part 1: General Information and Use-Case Definition*; ISO 15118-1 ED2:2019; International Organization for Standardization: Geneva, Switzerland, 2019.

18. International Electrotechnical Commission Home Page. Available online: https://www.iec.ch/dyn/www/f?p=103:23:3345849648066::::FSP_ORG_ID,FSP_LANG_ID:1255,25 (accessed on 5 September 2019).

19. International Organization for Standardization. *Road Vehicles–Vehicle to Grid Communication Interface–Part 8: Physical Layer and Data Link Layer Requirements for Wireless Communication*; ISO 15118-8:2018; International Organization for Standardization: Geneva, Switzerland, 2018.

20. Society of Automotive Engineers International. *Use Cases for Wireless Charging Communication for Plug-in Electric Vehicles*; SAE Information Report J2836/6; Society of Automotive Engineers International: Troy, MI, USA, 2013.

21. Society of Automotive Engineers International. *Communication between Wireless Charged Vehicles and Wireless EV Chargers*; SAE Recommended Practice J2847/6 (rev. 201508); Society of Automotive Engineers International: Troy, MI, USA, 2015.

22. Society of Automotive Engineers International. *Signaling Communication for Wirelessly Charged Electric Vehicles*; SAE Information Report J2931/6; Society of Automotive Engineers International: Troy, MI, USA, 2015.

23. International Organization for Standardization. *Information Technology–Open Systems Interconnection–Basic Reference Model: The Basic Model*; ISO 7489-1:1994; International Organization for Standardization: Geneva, Switzerland, 1994.

24. International Commission on Non-Ionizing Radiation Protection. Guidelines for limiting exposure totime-varying electric and magnetic fields for low frequencies (1 Hz–100 kHz). *Health Phys.* **2010**, *99*, 818–836.

25. Karalis, A.; Joannopoulos, J.D.; Soljačić, M. Efficient wireless non-radiative mid-range energy transfer. *Ann. Phys.* **2008**, *323*, 34–48. [CrossRef]

26. Wang, C.S.; Stielau, O.H.; Covic, G.A. Design considerations for contactless electric vehicle battery chager. *IEEE Trans. Ind. Electron.* **2005**, *52*, 1308–1314. [CrossRef]

27. Sallán, J.; Villa, J.L.; Llombart, A.; Sanz, J.F. Optimal design of ICPT systems applied to electric vehicle battery charge. *IEEE Trans. Ind. Electron.* **2009**, *56*, 2140–2149. [CrossRef]

28. Moradewicz, A.J.; Kazmierkowski, M.P. Contactless energy transfer system with FPGA-controlled resonant converter. *IEEE Trans. Ind. Electron.* **2010**, *57*, 3181–3190. [CrossRef]

29. Chopra, S.; Bauer, P. Analysis and design considerations for a contactless power transfer system. In Proceedings of the 33rd International Telecommunications Energy Conference, Amsterdam, The Netherlands, 9–13 October 2011.

30. Li, S.; Mi, C.C. Wireless power transfer for electric vehicle applications. *IEEE J. Emerg. Sel. Top. Power Electron.* **2015**, *3*, 4–17.

31. Stutzman, W.L.; Thiele, G.A. *Antenna Theory and Design*, 2nd ed.; John Wiley & Sons, Inc.: Hoboken, NJ, USA, 1998; p. 1.

32. Straw, R.D. *The ARRL Antenna Book*; The American Radio Relay League, Inc.: Newington, CT, USA, 1997; pp. 5-1–5-11.

33. DeVore, R.; Bohley, P. The electrically small magnetically loaded multiturn loop antenna. *IEEE Trans. Antennas Propag.* **1977**, *25*, 496–505. [CrossRef]

34. Pozar, D.M. *Microwave Engineering*, 2nd ed.; John Wiley & Sons, Inc.: Hoboken, NJ, USA, 1998; pp. 68–76, 300–303.

35. Duncan, B. *High Performance Audio Power Amplifiers*; Elsevier: Amsterdam, The Netherlands, 1996; pp. 147–148.

36. Alan, B. *Wireless Positioning Technologies and Applications*; Artech House: Norwood, MA, USA, 2016; pp. 147–167.

37. ANSYS Home Page. Available online: https://www.ansys.com (accessed on 7 September 2019).

38. Altair HyperWorks Home Page. Available online: https://altairhyperworks.com (accessed on 7 September 2019).

39. Seong, J.; Jang, J.; Koh, Y. A study of electric vehicle wireless charging system integration and vehicle alignment optimization. In Proceedings of the 30th International Electric Vehicle Symposium & Exhibition, Stuttgart, Germany, 9–11 October 2017.

40. VECTOR Home Page. Available online: https://www.vector.com (accessed on 7 September 2019).

41. International Telecommunication Union. *Technical and Operating Parameters and Spectrum Use for Short-Range Radiocommunication Devices*; ITU-R SM.2153-7; International Telecommunication Union: Geneva, Switzerland, 2019.

42. MathWorks Home Page. Available online: https://www.mathworks.com (accessed on 7 September 2019).

43. Rohde and Schwarz Home Page. Available online: https://www.rohde-schwarz.com/product/smc100a-productstartpage_63493-10181.html (accessed on 6 December 2019).

44. Rohde and Schwarz Home Page. Available online: https://www.rohde-schwarz.com/product/rte-productstartpage_63493-54848.html (accessed on 6 December 2019).

45. Chroma ATE Home Page. Available online: http://www.chromaate.com/product/EV_wireless_power_transfer_ATS.htm (accessed on 6 December 2019).